Electronic Supplementary Material (ESI) for Dalton Transactions.
This journal is © The Royal Society of Chemistry 2020

Electronic Supplementary Information

Identical anomalous Raman relaxation exponent in a family of Single Ion Magnets: towards reliable Raman relaxation determination

Gabriela Handzlik,[a] Michał Magott,[a] Mirosław Arczyński,[a] Alena M. Sheveleva,[b] Floriana Tuna,[b] Stanisław Baran[c] and Dawid Pinkowicz[a,]*

[a] Faculty of Chemistry, Jagiellonian University, Gronostajowa 2, 30-387 Kraków, Poland

[b] Department of Chemistry and Photon Science Institute, The University of Manchester, Oxford Road, Manchester M13 9PL, United Kingdom

[c] Marian Smoluchowski Institute of Physics, Jagiellonian University, Łojasiewicza 11, 30-348 Kraków, Poland

Table of contents

1. **Synthesis details**
2. **Elemental analysis**
3. **Single crystal X-ray diffraction**
4. **Shape calculations**
5. **Powder X-ray diffraction**
6. **Infrared spectroscopy**
7. **Inductively coupled plasma mass spectrometry and emission spectroscopy**
8. **Magnetic measurements**
9. **EPR spectroscopy**
10. **Ab initio calculations**

References

1. Synthesis details

Preparation of compounds

Erbium(III) nitrate pentahydrate (99.9%), ytterbium(III) nitrate pentahydrate (99.9%), yttrium(III) nitrate hexahydrate (99.9%) and methanol (analytical grade) were purchased from commercial sources (Sigma-Aldrich Co. and Avantor Performance Materials Poland S.A.) and used as received. N,N'-dioxophenanthroline was synthesized according to the reported procedure.[1] All operations were carried out under an ambient atmosphere.

Synthesis of [Er(phendo)$_4$](NO$_3$)$_3$·xMeOH (Er)

Methanol (16.0 g) was added to erbium(III) nitrate pentahydrate (0.10 mmol, 44.3 mg) and anhydrous phendo (0.45 mmol, 95.5 mg). The suspension was heated at reflux for 5 minutes with stirring until almost completely clear yellow solution was obtained. The hot mixture was filtered and left for crystallization in a closed vial. Pale yellow block crystals of **Er** were formed within 2 days. The crystals crack and fall apart immediately after being removed from the mother solution due to the crystallization solvent loss. Therefore, all measurements and experiments were performed for samples immersed in a small quantity of the mother liquor (PXRD, magnetic measurements) or in the mixture of toluene and methanol (EPR). After the magnetic measurements the samples were dried in vacuo over P_4O_{10} for 24 hours in order to remove the crystallization MeOH molecules from the structure. Sample was weighed (22.2 mg, yield: 18 %) and then it was left in ambient atmosphere for another 48 hours to allow the absorption of the H_2O molecules. It was weighed again and elemental analysis (EA) was performed: found C, 46.33; H, 3.032; N, 12.16. $C_{48}H_{32}ErN_{11}O_{17}\cdot(2.5H_2O)$ (1247.13 g/mol) requires C, 46.23; H, 2.99; N, 12.35.

Synthesis of [Yb(phendo)$_4$](NO$_3$)$_3$·xMeOH (Yb)

Synthesis of the **Yb** analogue was performed in as similar manner. Methanol (16.0 g) was added to ytterbium(III) nitrate pentahydrate (0.10 mmol, 44.9 mg) and anhydrous phendo (0.45 mmol, 95.5 mg). It was heated at reflux for 5 minutes with stirring and then immediately filtered. Pale yellow crystals of **Yb** were formed after approximately 2 days (48.6 mg, yield: 40 %). Similar procedure of drying/ H_2O absorption was applied for sample after magnetic measurement. Elemental analysis was performed after absorption of water; found C, 46.39; H, 2.953; N, 12.24. $C_{48}H_{32}YbN_{11}O_{17}\cdot(2.5H_2O)$ (1252.91 g/mol) requires C, 46.01; H, 2.98; N, 12.30.

Syntheses of the solid state dilution compounds: Er2% and Yb2%

The solid state dilution of [Ln(phendo)$_4$](NO$_3$)$_3$·xMeOH (Ln = Er or Yb) within the diamagnetic yttrium(III) matrix was performed at the synthesis stage by mixing the appropriate amounts of $Ln^{III}(NO_3)_3\cdot5H_2O$ (2nd column in Table S1) and $Y^{III}(NO_3)_3\cdot6H_2O$ (3rd column in Table S1) in MeOH to achieve the intended 2% molar fraction of Ln^{III}. The Ln^{III}/Y^{III} MeOH solution was added to the hot methanol suspensions of the ligand (4th column in Table S1). After short stirring under reflux, solution was filtered and left for crystallization for 2 days. Solid state solutions with Y^{III} ware done thanks to confidence that yttrium(III) generate analogical structure with phendo as lanthanide ions what was proved earlier.[2] The isostructural character of the obtained samples with the rest of the series was confirmed by powder X-ray diffraction experiments (Figure S3). The actual molar fractions of Ln^{III} and Y^{III} in the obtained samples were determined by ICP-MS and ICP-OES analysis, respectively (see the ICP section below).

Table S1. Amounts of the substrates used to prepare the solid state diluted samples: **Er2%**, **Yb2%**, **Er0.3%**, **Er5%**, **Yb0.3%**, **Yb1%**.

	$Ln(NO_3)_3\cdot5H_2O$ (Ln = Dy/Er/Yb)	**$Y(NO_3)_3\cdot6H_2O$**	**phendo**
Er2%	2.00 mL of the following solution: 20.8 mg (0.047 mmol) in 6 mL of MeOH	15.0 mL of the following solution: 294.9 mg (0.770 mmol) in 15.0 mL MeOH	150 mL of the following solution: 749.1 mg (3.53 mmol) in 150 mL MeOH
Yb2%	2.00 mL of the following solution: 21.1 mg (0.047 mmol) in 6 mL of MeOH		
Er0.3%	0.50 mL of the following solution: 12.4 mg (0.028 mmol) in 25 mL of MeOH	6.0 mL of the following solution: 71.6 mg (0.187 mmol) in 6.0 mL MeOH	30 mL of the following solution: 179.1 mg (0.844 mmol) in 30 mL MeOH
Yb0.3%	0.50 mL of the following solution: 12.6 mg (0.028 mmol) in 25 mL of MeOH		
Er1%	1.00 mL of the following solution: 13.7 mg (0.031 mmol) in 10 mL of MeOH	10.0 mL of the following solution: 118.4 mg (0.309 mmol) in 10.0 mL MeOH	50 mL of the following solution: 298.4 mg (1.406 mmol) in 50 mL MeOH
Yb5%	2.50 mL of the following solution: 56.1 mg (0.125 mmol) in 10 mL of MeOH	22.5 mL of the following solution: 227.5 mg (0.594 mmol) in 22.5 mL MeOH	100 mL of the following solution: 596.9 mg (2.813 mmol) in 100 mL MeOH

2. Elemental analysis

Elemental analyses were performed using ELEMENTAR Vario Micro Cube CHNS analyser. Samples for elemental analyses (**Er**, **Yb**) were dried in vacuo over P_4O_{10} for 24 hours and then left under ambient conditions (23°C, 63±5% relative humidity) for 48 hours to allow the absorption of H_2O molecules.

3. Single crystal X-Ray diffraction

The single crystal X-ray diffraction (scXRD) data for **Er** and **Yb** were collected on a Bruker D8 Quest Eco three-circle diffractometer equipped with a Photon50 CMOS detector, a MoKα sealed tube X-ray radiation source and a Triumph monochromator. Details of the measurements and refinements are presented in Table S2. Data reduction, scaling and absorption corrections (multi-scan) were carried out using SAINT and SADABS, which are the part of Apex3 suite of programs. Structures were determined by direct methods (intrinsic phasing) using Apex3 software (ShelXT) and OLEX2 (ShelXT).[3,4] All non-hydrogen atoms were refined anisotropically except the oxygen atoms of the nitrate anions. Least-squares refinement of parameters with approximation to the normal matrix were made by minimizing the function $\Sigma w(|F_o|-|F_c|)^2$, where F_o and F_c are the observed and calculated structure factors. For each compound the structures were determined at low temperature (120 or 100 K; main structural model) and at room temperature (supporting structural model) which was used for comparison with the experimental PXRD patterns recorded for bulk samples at room temperature.

Table S2. Crystal structure solution and refinement parameters for [Er(phendo)$_4$](NO$_3$)$_3$·xMeOH (**Er**) and [Yb(phendo)$_4$](NO$_3$)$_3$·xMeOH (**Yb**) at low temperature (120 K or 100 K) and at room temperature (293 K).

Formula	$C_{48}H_{32}ErN_{11}O_{17}$		$C_{48}H_{32}YbN_{11}O_{17}$	
M_r/g mol^{-1}	1202.10		1207.88	
T/*K*	120(2)	293(2)	100(2)	293(2)
CCDC	1965558	1965559	1965560	1965556
Crystal system	Tetragonal			
Space group	*I*4/*m*			
a/Å	15.2889(14)	15.3972(16)	15.2258(10)	15.354(8)
c/Å	22.186(2)	22.418(4)	22.1833(16)	22.421(15)
V/Å^3	5185.9(11)	5314.8(14)	5142.6(8)	5286(6)
Z	4	4	4	4
ρ_{calc}/g cm^{-3}	1.540	1.502	1.560	1.518
μ/mm^{-1}	1.700	1.66	1.901	1.849
F(000)	2404	2404	2412	2412
Crystal size/mm^3	0.18 x 0.18 x 0.11	0.40 x 0.40 x 0.23	0.30 x 0.18 x 0.13	0.60 x 0.35 x 0.35
Radiation	Mo Kα (λ = 0.71073 Å)			
2θ range/°	2.7-26.1	2.6-26.4	2.6-28.2	2.6-27.6
Reflections collected	27713	22766	15482	30907
Independent reflections	2628	2793	3258	3114
R_{int}	0.042	0.067	0.030	0.030
restrains/parameters	41/190	47/203	32/193	29/186
$R[F_o > 2\sigma(F_o)]$	0.061	0.049	0.043	0.036
$wR(F^2)$	0.191	0.142	0.131	0.113
GOF on F^2	1.191	1.050	1.082	1.102
$\Delta\rho_{max}$, $\Delta\rho_{min}$ /e Å^{-3}	2.72/-3.52	2.62/-1.66	2.53/-3.52	1.43/-1.67
Completeness/%	99.7	99.8	99.5	99.6

Table S3. Quantitative description of voids in the structures. Platon squeeze void probe radius is 1.2 Å.

	Er 120 K	**Yb** 100 K
Solvent accessible volume / Å^3	953	948
electrons	276	286
% of unit cell volume	18.4	18.4
MeOH molecules (70 Å^3 per MeOH molecule)	13.6	13.5

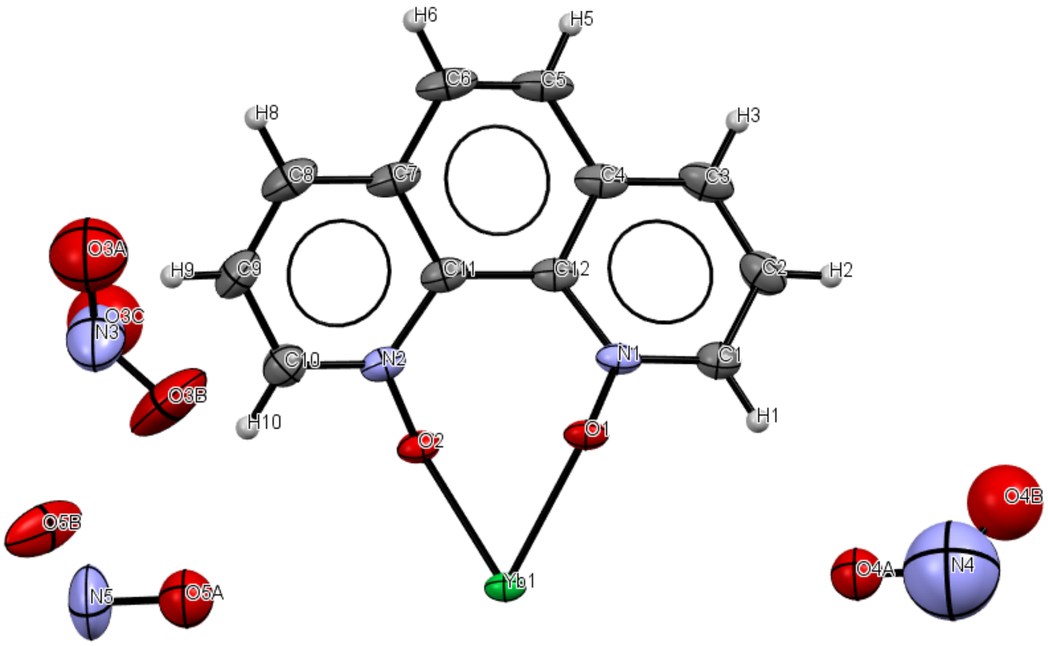

Figure S1. Asymmetric unit of [Ln(phendo)$_4$](NO$_3$)$_3$·xMeOH depicted on the example of Yb-based compound measured at 100 K. Thermal ellipsoids are shown at the 50 % probability level.

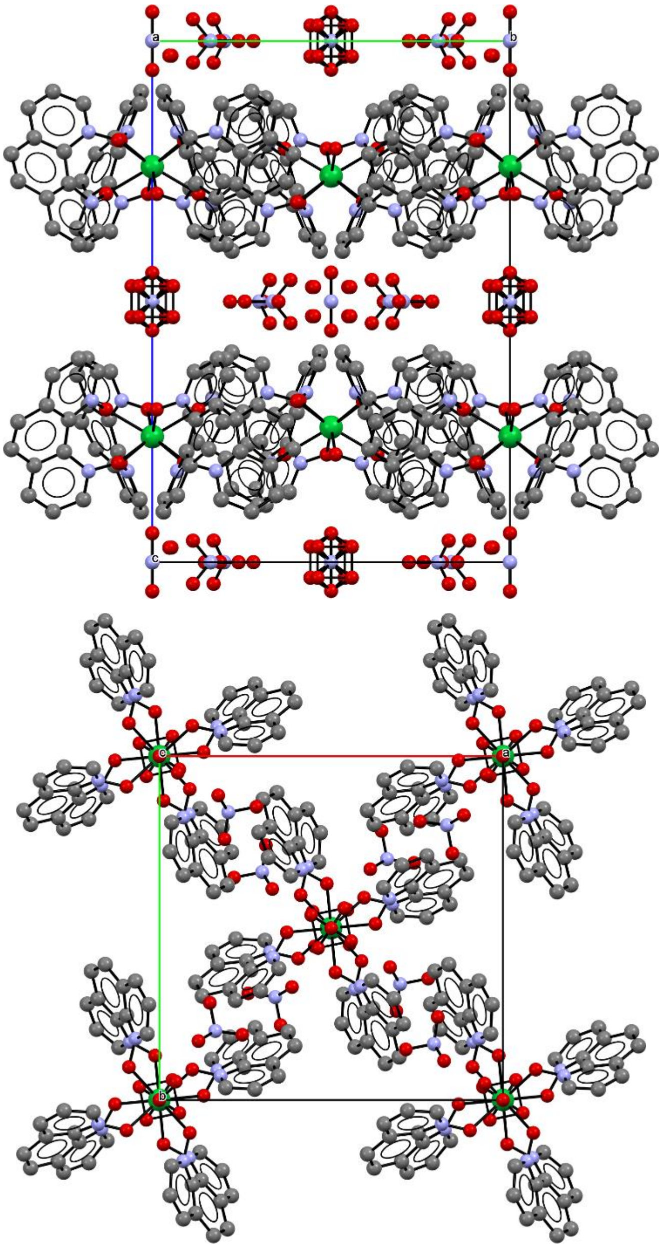

Figure S2. Crystal packing of [Yb(phendo)$_4$](NO$_3$)$_3$·xMeOH along *a* (top) and *c* (bottom) directions. Hydrogen atoms are omitted for the sake of clarity.

4. SHAPE Calculations and geometry analysis

Continuous Shape Measure Analysis for coordination spheres of Er^{III} and Yb^{III} was performed using SHAPE software.[5] In each case the coordination geometry around the respective lanthanide(III) ion was close to square antiprism (values for D_{4d} symmetry are closest to zero). The results of geometry analysis is presented in the Table S4 below. It contains results from SHAPE analysis as well as analysis of crucial angles (φ and θ) and distances (Ln1-O1 and Ln1-O2) for distortion of square antiprism. Analysis of separation of lanthanides centres in the structure is also presented below as distances between the closest neighbours.

Table S4. Results of the SHAPE analysis for coordination spheres of the metal ions in **Er** and **Yb** with selected angles and distances in the structures.

			Er (120 K)	**Er** (293 K)	**Yb** (100 K)	**Yb** (293 K)	**Perfect square antiprism**
Symmetry of Ln^{III} coordination sphere	Cube (CU-8) O_h		8.411	7.906	8.060	7.984	-
	Square antiprism (SAPR-8) D_{4d}		0.328	0.445	0.367	0.412	0.000
	Triangular dodecahedron (TDD-8) D_{2d}		2.482	2.438	2.404	2.429	-
	Biaugmented trigonal prism (BTPR-8) C_{2v}		2.480	2.675	2.549	2.615	-
Angles /°	φ		37.82	36.48	37.17	36.77	45
	θ	beside O1	59.73	59.99	59.52	59.75	54.7
		beside O2	60.83	60.61	60.53	60.68	54.7
Distances /Å	Ln1-O1		2.302(4)	2.320(3)	2.289(2)	2.293(2)	-
	Ln1-O2		2.305(4)	2.310(3)	2.283(3)	2.283(2)	-
Ln···Ln distance /Å	along *c* direction		10.702 11.483	10.790 11.628	10.693 11.490	10.776 11.645	-
	along *a* direction		15.289	15.397	15.226	15.354	-
	along diagonal in *ab*-plane		10.818	10.896	10.774	10.866	-

5. Powder X-Ray diffraction

The fact that all measured samples are isostructural was confirmed by powder X-ray diffraction (PXRD; Figure S3). PXRD experiments were carried out using Bruker D8 Advance Eco diffractometer (CuKα radiation and graphite monochromator) at ambient temperature for well-ground samples in mother solutions loaded into a narrow diameter borosilicate-glass tube (0.7 mm in diameter). Reflections on all experimental and simulated PXRD diffraction patterns are in very good agreement confirming the purity and identity of the samples.

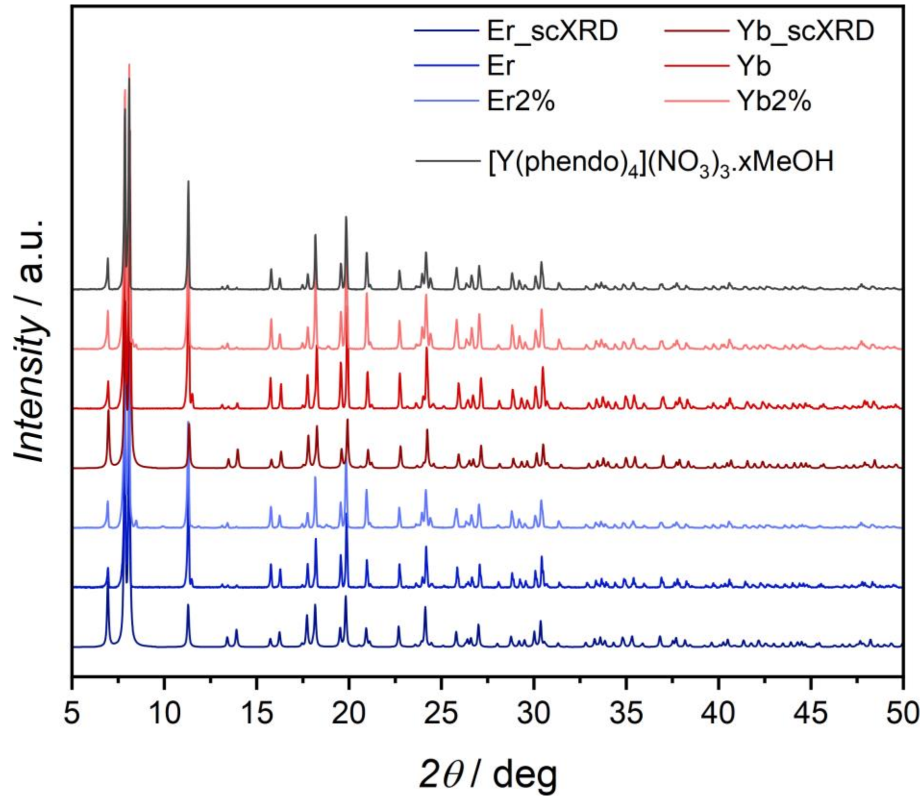

Figure S3. Comparison of the PXRD patterns simulated from sc-XRD measurements (Er_scXRD and Yb_scXRD) and experimental ones for pure lanthanide compounds (**Er**, **Yb, Y**) and for solid state diluted samples (**Er2%**, **Yb2%**).

6. Infrared spectroscopy

Infrared spectra (Figure S4) were collected on Nicolet iS 5 FT-IR microscope in the 4000 - 700 cm^{-1} range. Below 1800 cm^{-1} every sample (**Er**, **Yb** and Y analog) exhibits bands typical for the phendo ligand (orange line). The broad band located around 1330-1350 cm^{-1} is assigned to the NO_3^- vibrations and confirms its presence in $[Ln(phendo)_4](NO_3)_3 \cdot xMeOH$ as the counterion.

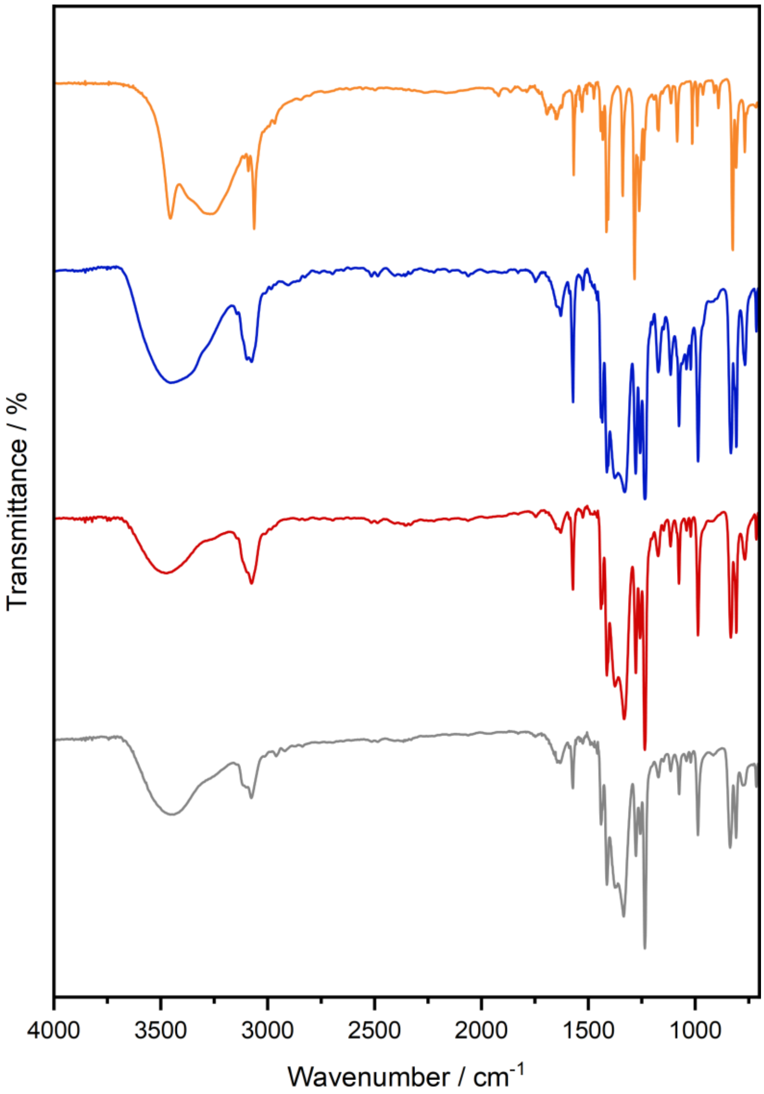

Figure S4. IR spectra of phendo (orange), **Er** (blue), **Yb** (red) and **Y** (grey).

7. Inductively coupled plasma mass spectrometry and emission spectroscopy

Amounts of the Ln^{III} (Er^{III} or Yb^{III}) ions in the solid state diluted compounds **Er2%** and **Yb2%** were determined experimentally by inductively coupled plasma mass spectrometry (Perkin Elmer, ICP-Q-MS Elan DRC-e spectrometer). For both lanthanide ions four isotopes were taking into account (Er: 166, 167, 168 and 170; Yb: 171, 172, 173 and 174). Amounts of Y^{III} ions in these samples were determined by inductively coupled plasma atomic emission spectroscopy (Perkin Elmer, ICP-OES Optima 2100DV). Monitored wave lengths in experiment for Y^{III} determination: 224.303 nm, 324.227 nm, 360.073 nm and 361.104 nm. The actual Ln^{III} molar fractions presented in Table S5 are consistent with the anticipated values based on the reaction stoichiometry. The analysis confirms the high solid state dilution of these samples.

Table S5. Results of the ICP-MS and ICP-OES analysis for Ln^{III} and Y^{III} ions, respectively, in **Er2%** and **Yb2%**.

sample	Ln^{III} / µg/mg	Y^{III} / µg/mg	Ln^{III} molar fraction / %
Er2%	2.68(1)	69.2(5)	2.02
Yb2%	2.62(1)	70.9(3)	1.86

These results were obtained using the equipment purchased thanks to the financial support of the European Regional Development Fund in the framework of the Polish Innovation Economy Operational Program (contract no. POIG.02.01.00-12-023/08).

8. Magnetic Measurements

The direct current (DC) and alternating current (AC) magnetic measurements for all samples were performed using Quantum Design MPMS-3 Evercool magnetometer. Additionally AC magnetic measurements for diluted samples (**Er2%** and **Yb2%**) were performed also on Physical Property Measurement System PPMS (in the frequency range 10-10000 Hz) in order to extend the frequency range and characterise the magnetic relaxation to higher temperatures.

Each sample was ground to a powder and loaded into a delrin container with a minimal amount of the mother solution (in methanol). The container was sealed suing a delrin plug and fit into a long plastic straw with two 3 cm delrin rods above and below the container. The samples were always cooled below the freezing point of the mother liquor in the absence of the magnetic field to avoid the orientation of the crystallites. The data of magnetic susceptibility were corrected for the diamagnetic contributions of the sample holder and the diamagnetism of the samples using Pascal constants.[6]

DIRECT CURENT MAGNETIC MEASUREMENTS

DC magnetic measurements were performed in order to investigate the static magnetic behaviour of the samples and also to estimate the amount of lanthanide(III) ions in diluted samples. The molar magnetic susceptibilities of **Er** and **Yb** were investigated in an applied magnetic field of 0.1 T in the 2.0 – 200 K range. The temperature dependence of the $\chi_M T$ products is given in Figure S5. The $\chi_M T$ values at 200 K for these compounds are presented in Table S6 and they are in good agreement with the theoretical values for the isolated Ln^{III} ions. In every case the $\chi_M T$ product decreases with decreasing temperature as expected for lanthanide(III)-based compounds due to thermal depopulation of the m_J states. The magnetization vs field dependences for **Er** and **Yb** (at T = 1.8 K or 2.0 K) are presented in Figure S6 below. In every case the magnetisation does not reach saturation value at external magnetic field of 5 T. The obtained values of magnetisation at the maximum accessible field are presented in Table S6 and compared with the theoretical ones for free ions. The experimental values are lower than those expected for free ions because of m_J splitting in the ligand field and resulting Boltzmann depopulation of the excited states. The $M(H)$ dependences for **Er2%** and **Yb2%** (at T = 2.0 K) were compared with plots for pure samples **Er** and **Yb** in order to estimate the amount of the paramagnetic ions in the diluted samples, but the exact concentrations (molar fractions) were determined by ICP-MS (see section 7 above).

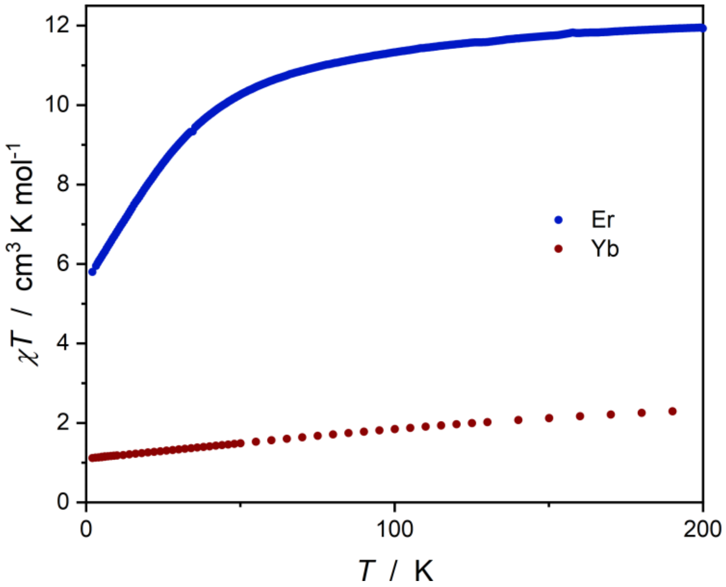

Figure S5. Temperature dependence of the χT product for **Er** and **Yb** in an applied magnetic field of 0.100 T in the 2.0 – 200 K range.

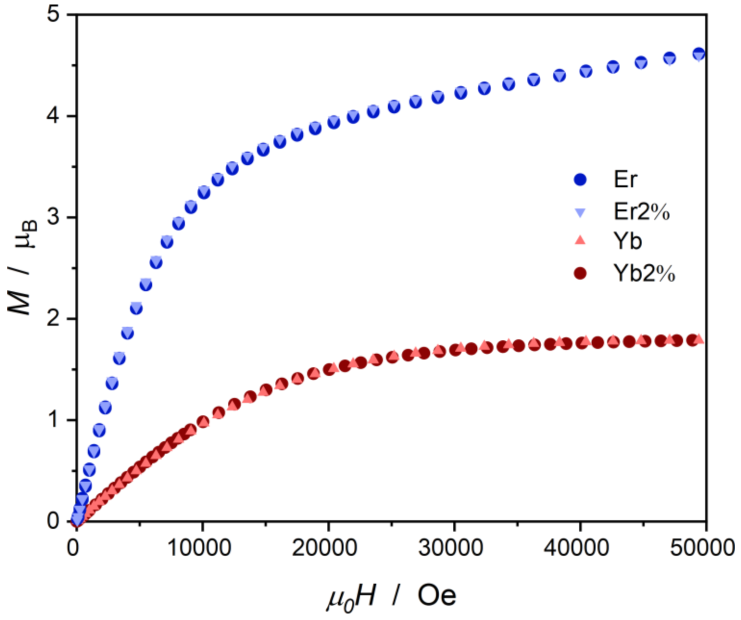

Figure S6. Comparison of field dependence of the molar magnetization measured for **Er** (2.0 K), **Er2%** (2.0 K), **Yb** (1.8 K) and **Yb2%** (2.0 K).

Table S6. Theoretical values of $\chi_M T$ and M_{sat} for free lanthanide(III) ions and experimental values of $\chi_M T$ and M_{sat} for **Er** and **Yb**.

	$\chi_M T$ / cm^3 K mol^{-1}			M_{sat} / μ_B	
	theoretical (RT)	**exp. (200 K)**	**exp. (2.0 K)**	**theoretical**	**exp. (at 5 T)**
Er	11.48	11.93	5.80	9.0	4.6
Yb	2.57	2.33	1.12	4.0	1.8

ALTERNATING CURENT MAGNETIC MEASUREMENTS

Dynamic magnetic properties of **Er**, **Er2%**, **Yb** and **Yb2%** are presented in Figures S7-S18. In-phase and out-of-phase data from Quantum Design MPMS-3 Evercool magnetometer (in the range of 1 - 1000 Hz) are presented as circles and data from the Physical Property Measurement System PPMS (in the frequency range 10-10000 Hz) are presented as stars. Solid lines in every figure are best fits to the generalised Debye model. One can find equations for one or two modified Debye functions in ref. 7.[7] The values of relaxation times τ and Cole-Cole parameters α (describing distribution of the time constants around τ) for every fitted curve are presented in Tables S7-S14). Analysis of dynamic magnetic behaviour of these samples is described in the main text.

AC magnetic properties of undiluted Er

Frequency dependence of the out-of-phase (χ'') magnetic susceptibility of **Er** shows two maxima in the 1-1000 Hz range under small applied DC fields 150 – 5000 Oe (T = 1.8 K; Figure S7, Table S7). The maximum at low frequencies shifts from around 20 Hz to below 1 Hz with increasing magnetic field. There is contribution of QTM which is visible on $\tau(H)$ dependency in Figure S9a. The second maximum corresponding to the faster relaxation process is clearly visible at low DC fields up to 1000 Oe and noticeably changes its position by moving to frequencies higher than 1000 Hz above 1250 Oe. The observed behavior of undiluted **Er** in the 1-1000 Hz frequency window limits the possibility to study the corresponding field dependencies of the relaxation times τ thoroughly (Figure S9c).

Temperature dependence of the AC magnetic susceptibility was measured at two optimal DC fields to analyze the temperature dependence of the slower (H_{DC} = 2000 Oe) and faster (H_{DC} = 200 Oe) relaxation processes in a possibly wide temperature range. The χ'' maximum of the slower relaxation process for **Er** is almost temperature independent and vanishes completely at 3.1 K (Figure S8, Table S8, Figure S9d). The second maximum depends on temperature, but is visible only up to 2.9 K in the 1 - 1000 Hz window which prevented the proper analysis of the ln $\tau(T^{-1})$ dependence (Figure S8, Table S8, Figure S9b).

AC magnetic properties of diluted Er2%

The solid state diluted compound **Er2%** enables the observation of only one clear χ'' maximum that varies with the magnetic field (Figures S10, S12a, Table S9). The temperature variation of the $\chi',\chi''(\nu)$ dependencies under the optimal magnetic field of H_{DC} = 400 Oe is presented in Figure S11 (Table S10). The corresponding relaxation process is slightly slower than in the undiluted **Er** (Figure S12b).

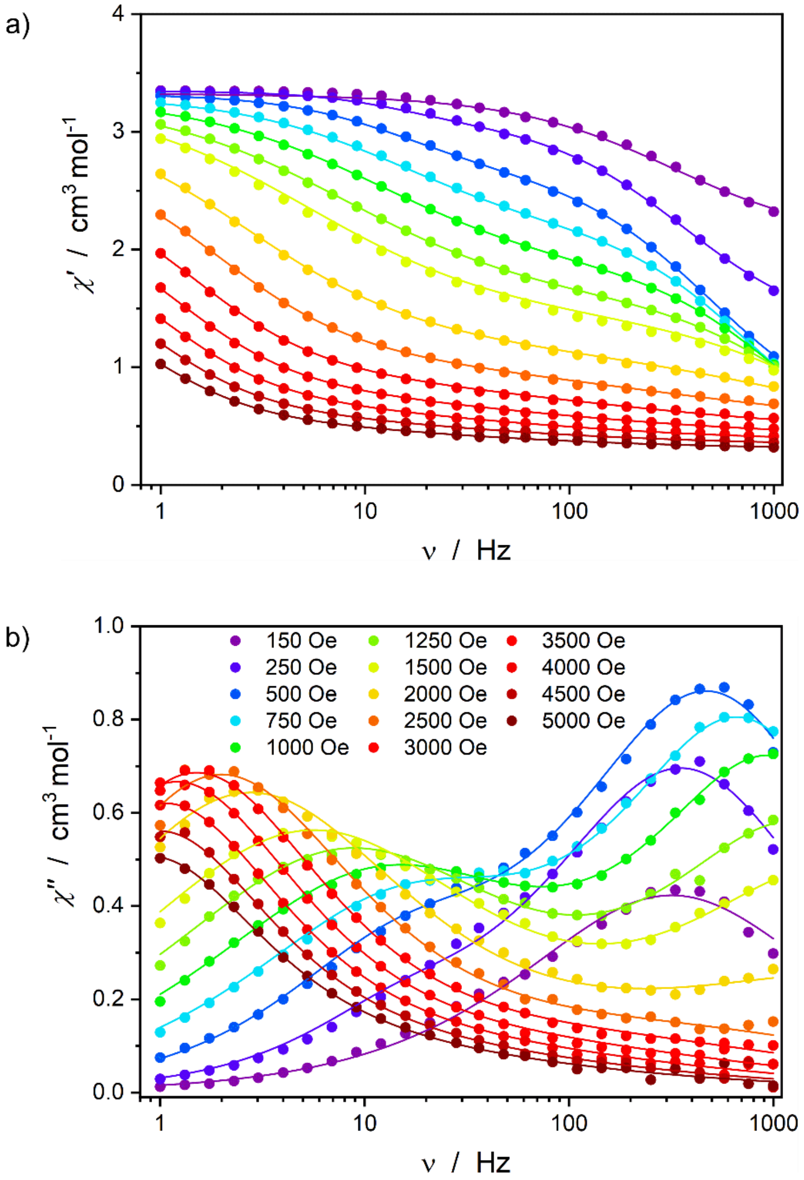

Figure S7. In-phase (χ') and out-of-phase (χ'') AC susceptibilities for **Er** at 1.8 K measured in various fields H_{DC}. Values of α and τ parameters are presented in Table S7.

Table S7. Values of α and τ from fitting two modified Debye functions to $\tau(\nu)$ dependencies for **Er** at 1.8 K.

H / Oe	**α_1**	**τ_1 / s**	**α_2**	**τ_2 / s**
150	0.251(38)	$5.00(28)\cdot10^{-4}$		
250	0.203(19)	$4.41(11)\cdot10^{-4}$		
500	0.207(15)	$3.19(6)\cdot10^{-4}$		
750	0.153(16)	$2.19(5)\cdot10^{-4}$	0.270(14)	0.0110(5)
1000	0.156(13)	$1.52(4)\cdot10^{-4}$	0.317(7)	0.0139(3)
1250	0.192(31)	$1.15(10)\cdot10^{-4}$	0.338(11)	0.0203(5)
1500			0.345(30)	0.0303(19)
2000			0.294(18)	0.0602(17)
2500			0.212(25)	0.0833(25)
3000			0.175(20)	0.1097(25)
3500			0.159(26)	0.1363(41)
4000			0.134(28)	0.1550(49)
4500			0.096(36)	0.1639(58)
5000			0.096(46)	0.1821(89)

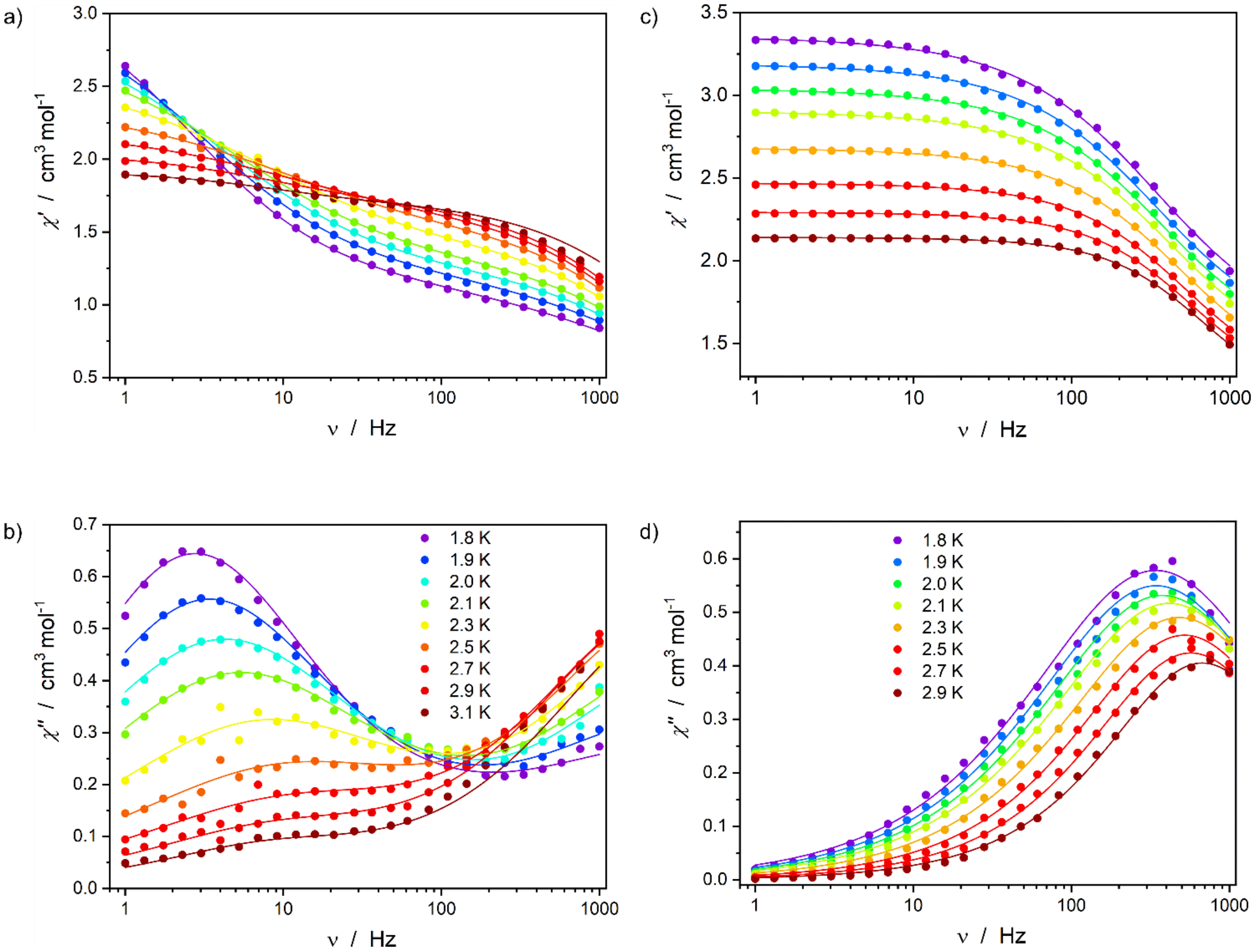

Figure S8. Temperature dependence of $\chi'(\nu)$ and $\chi''(\nu)$ for **Er:** a,b) in a 2000 Oe DC field (slow process) and c,d) in a 200 Oe DC field (fast process). Values of α and τ parameters are presented in Table S8.

Table S8. Values of α and τ from fitting two or one modified Debye functions to $\tau(\nu)$ dependencies for **Er**: in H_{DC} = 2000 Oe – α_1, τ_1 and in H_{DC} = 200 Oe - α, τ, respectively.

T / K	**α_1**	**τ_1 / s**	**α_2**	**τ_2 / s**
1.8	0.303(17)	0.0599(17)	0.299(9)	$4.65(16)\cdot10^{-4}$
1.9	0.337(15)	0.0491(14)	0.281(10)	$4.62(17)\cdot10^{-4}$
2.0	0.381(15)	0.0393(13)	0.273(9)	$4.25(14)\cdot10^{-4}$
2.1	0.391(11)	0.0321(8)	0.268(7)	$3.82(10)\cdot10^{-4}$
2.3	0.408(29)	0.0223(19)	0.247(7)	$3.31(8)\cdot10^{-4}$
2.5	0.417(34)	0.0167(22)	0.208(6)	$3.06(7)\cdot10^{-4}$
2.7			0.174(7)	$2.79(6)\cdot10^{-4}$
2.9			0.147(6)	$2.36(5)\cdot10^{-4}$

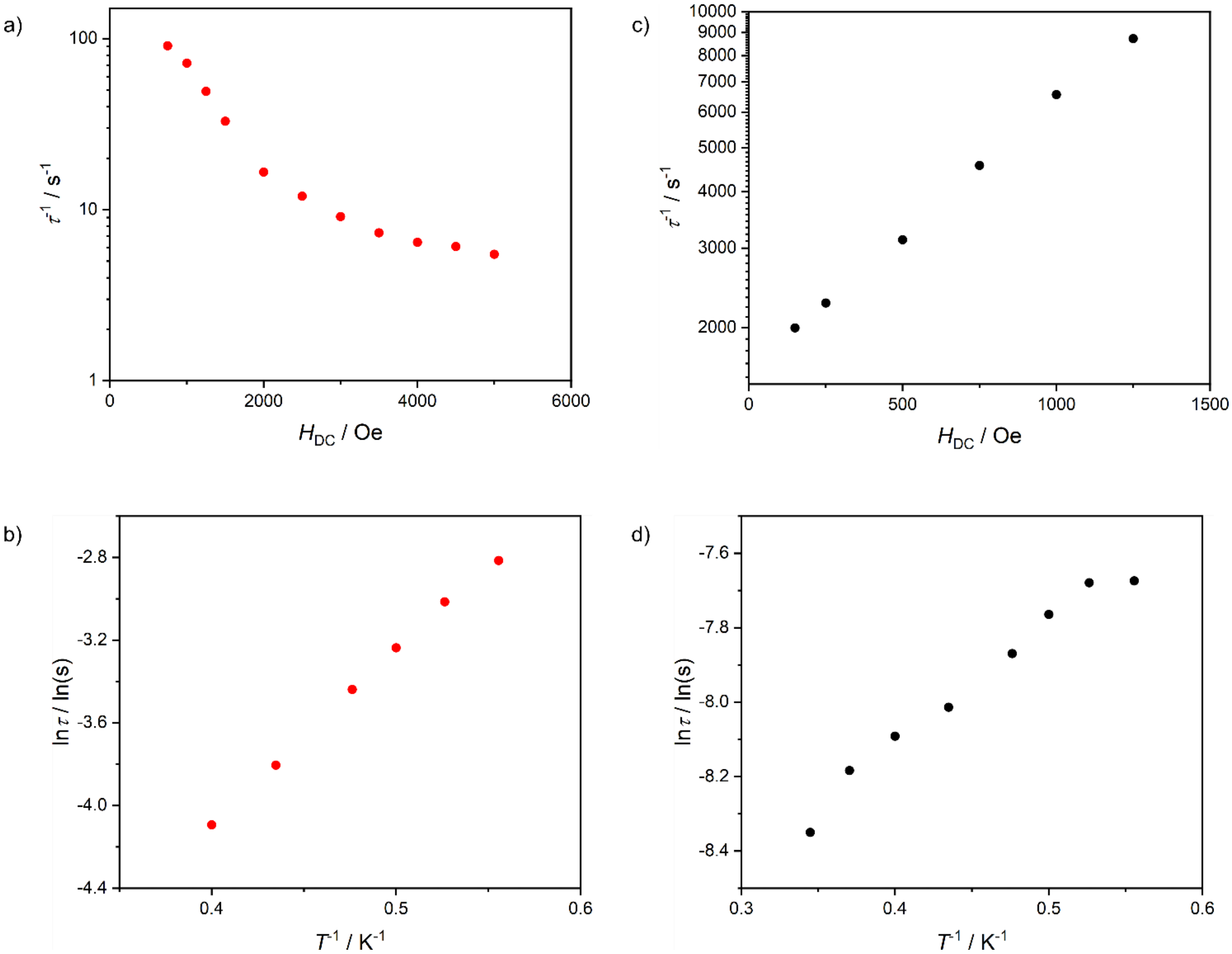

Figure S9. Field dependences of $1/\tau$ for **Er** at 1.8 K (150 – 5000 Oe) for a) slower (red) and c) faster (black) processes. Thermal dependences of lnτ for b) slower (red) and d) faster (black) processes for **Er** under 2000 Oe and 200 Oe, respectively.

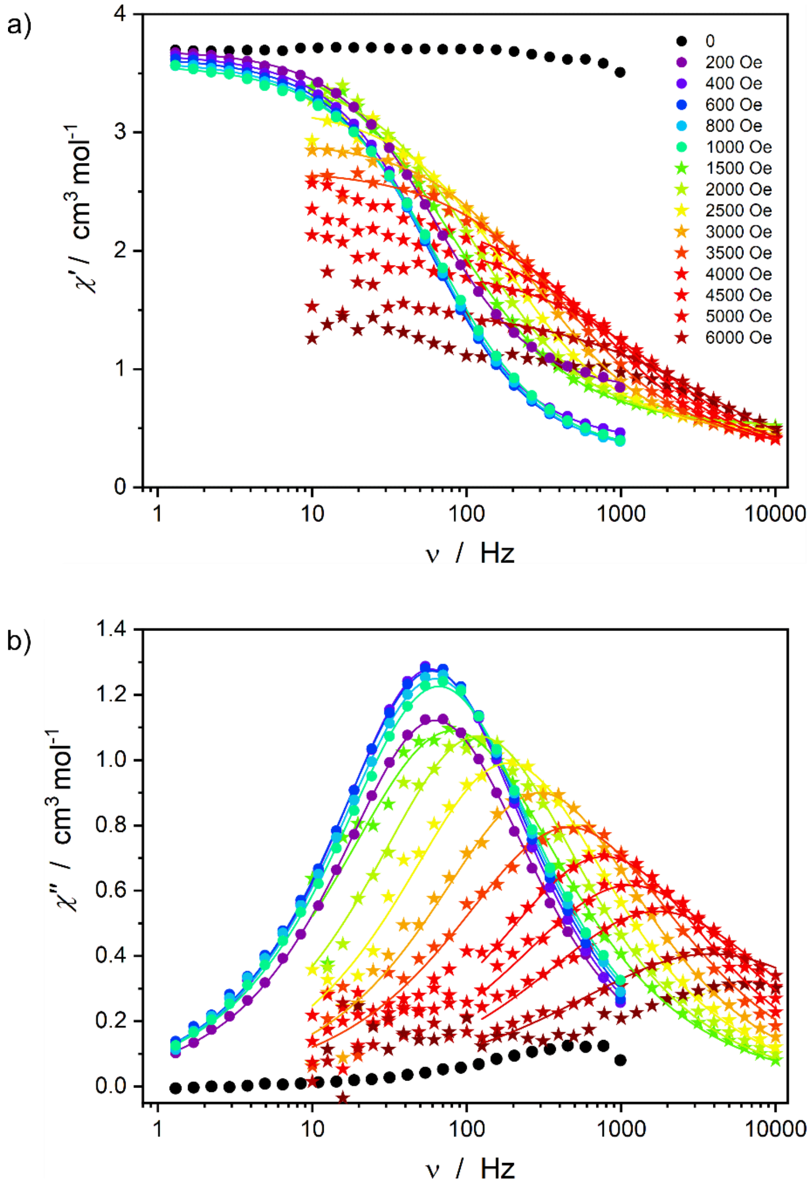

Figure S10. In-phase (χ') and out-of-phase (χ″) AC susceptibilities for **Er2%** at 1.8 K (circles) and at 1.9 K (stars). Values of α and τ parameters are presented in Table S9.

Table S9. Values of *α* and *τ* from fitting one modified Debye function to *τ*(*ν*) dependencies for **Er2%** at 1.8 K.

***H* / Oe**	***α***	***τ* / s**
200	0.164(3)	0.00254(1)
400	0.162(3)	0.00272(1)
600	0.176(3)	0.00267(2)
800	0.185(3)	0.00255(1)
1000	0.191(3)	0.00241(1)
1500	0.248(10)	0.00197(5)
2000	0.216(12)	0.00134(4)
2500	0.216(11)	$8.59(20)\cdot10^{-4}$
3000	0.219(11)	$5.34(13)\cdot10^{-4}$
3500	0.254(12)	$3.45(9)\cdot10^{-4}$
4000	0.232(8)	$2.05(3)\cdot10^{-4}$
4500	0.270(11)	$1.39(3)\cdot10^{-4}$
5000	0.290(11)	$9.22(22)\cdot10^{-5}$
6000	0.379(15)	$4.16(24)\cdot10^{-5}$

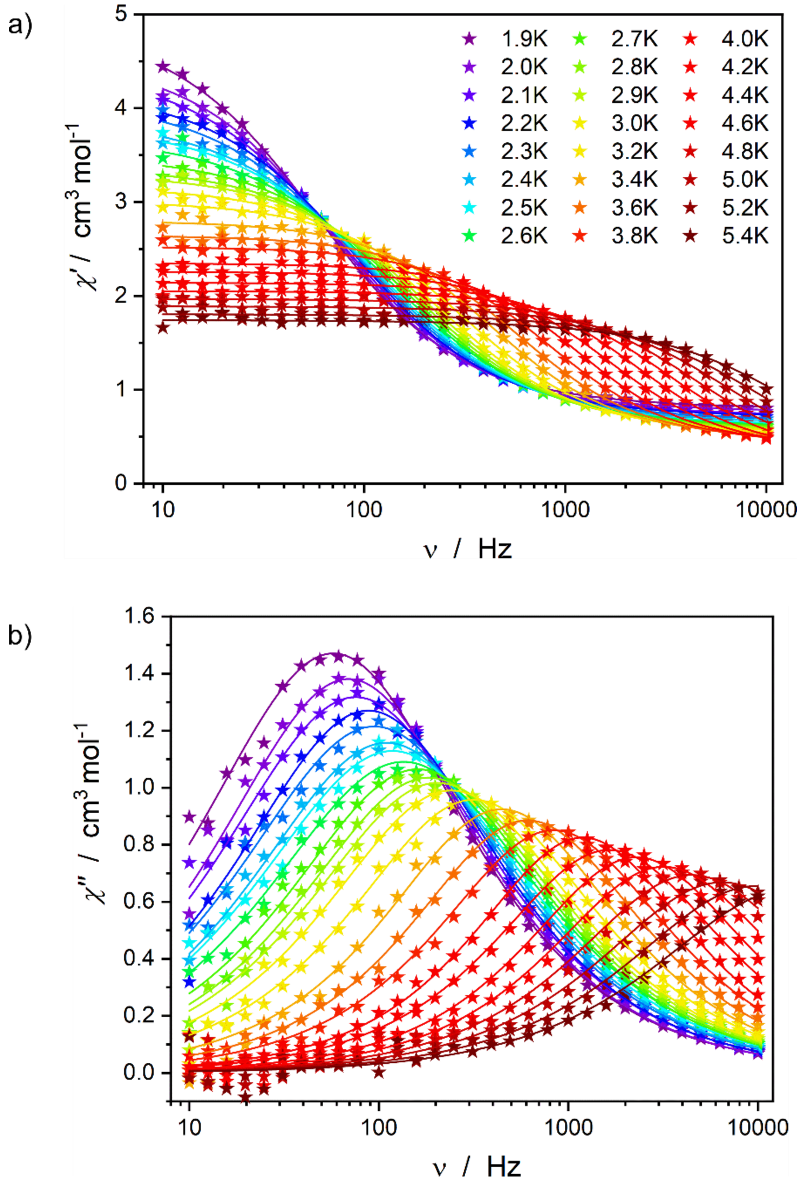

Figure S11. Temperature dependence of $\chi'(\nu)$ and $\chi''(\nu)$ for **Er2%** (10-10000 Hz; H_{DC} = 400 Oe). Values of α and τ parameters are presented in Table S10.

Table S10. Values of α and τ from fitting one modified Debye function to $\tau(\nu)$ dependencies for **Er2%** in H_{DC} = 400 Oe.

T / K	α	τ / s
1.9	0.213(5)	0.00277(3)
2.0	0.199(5)	0.00230(3)
2.1	0.217(5)	0.00211(2)
2.2	0.202(7)	0.00181(3)
2.3	0.220(6)	0.00168(2)
2.4	0.215(5)	0.00145(2)
2.5	0.226(6)	0.00135(2)
2.6	0.223(7)	0.00118(2)
2.7	0.198(8)	$9.90(15)\cdot10^{-4}$
2.8	0.193(6)	$8.68(11)\cdot10^{-4}$
2.9	0.192(8)	$7.81(13)\cdot10^{-4}$
3.0	0.179(5)	$6.61(7)\cdot10^{-4}$
3.2	0.169(6)	$5.03(6)\cdot10^{-4}$
3.4	0.142(9)	$3.58(6)\cdot10^{-4}$
3.6	0.135(8)	$2.61(4)\cdot10^{-4}$
3.8	0.136(7)	$1.91(2)\cdot10^{-4}$
4.0	0.102(11)	$1.33(3)\cdot10^{-4}$
4.2	0.126(7)	$9.67(13)\cdot10^{-5}$
4.4	0.114(12)	$6.96(17)\cdot10^{-5}$
4.6	0.126(11)	$4.99(12)\cdot10^{-5}$
4.8	0.144(13)	$3.56(13)\cdot10^{-5}$
5.0	0.167(21)	$2.46(17)\cdot10^{-5}$
5.2	0.187(21)	$1.64(15)\cdot10^{-5}$
5.4	0.209(35)	$1.09(23)\cdot10^{-5}$

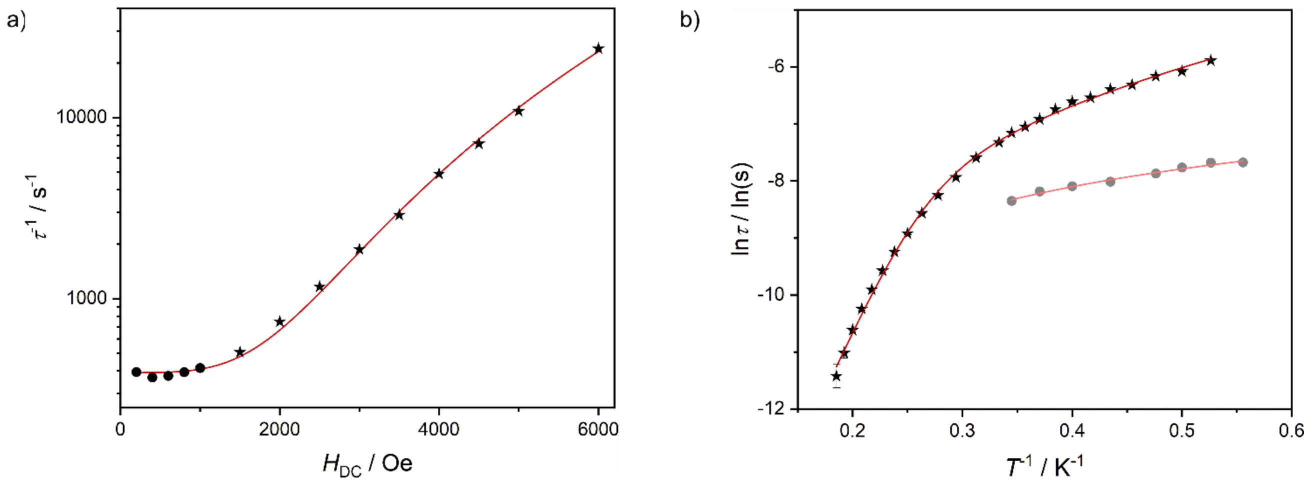

Figure S12. a) Field dependence of τ for **Er2%** at 1.8 K (0 – 1000 Oe) and at 1.9 K (1500 - 6000 Oe). b) Thermal dependence of τ for faster processes for **Er** in 200 Oe (grey circles, light red line) and for **Er2%** in 400 Oe DC field (black stars, dark red line).

Magnetic properties of undiluted Yb

Frequency dependence of the out-of-phase (χ'') magnetic susceptibility of **Yb** also shows two maxima in the 1-1000 Hz range under small applied DC fields 500 – 5000 Oe (T = 1.8 K; Figures S13, Table S11). The maximum corresponding to the slower process is clearly below 1 Hz in the whole magnetic field range. The maximum corresponding to the faster process is clearly visible below 2000 Oe but shifts above 1000 Hz above this field. Therefore, the analysis of the $\tau(H)$ dependencies for **Yb** could only be performed in a narrow magnetic field range and its usefulness is limited (Figure S15).

Temperature dependence of the $\chi_{AC}(\nu)$ was measured at the optimal DC field of 500 Oe (Figure S14, Table S12) to analyze the fast relaxation process for **Yb** in a possibly wide temperature range (the slow relaxation is inaccessible in the 1- 1000 Hz range). $\chi_{AC}(\nu)$ shows only one maximum (up to 3.1 K) which shows clear temperature dependence. However, similarly to **Er** the 1-1000 Hz frequency range is not sufficient to collect enough data for reliable analysis of the temperature dependence of the relaxation time $\ln\tau(T^{-1})$.

AC magnetic properties of diluted Yb2%

Surprisingly, the diamagnetic dilution leads to the $\chi_{AC}(\nu)$ suggesting the presence of two unresolved maxima in the range of 10 – 10000 Hz (Figure S16, Table S13). We observe these two maxima of χ'' up to the DC field of around 4000 Oe. In higher fields just one clear signal is distinguishable. In very small DC fields (200-300 Oe) maximum from faster relaxation process is a bit stronger than the other, but situation reverses quickly in higher fields (≥ 400 Oe) and maximum from faster relaxation process starts to disappear. Up to around 3000 Oe both maxima almost do not change their frequency, but over 3000 Oe, when one of them disappears in the slope of the other, the second one starts to shift clearly to the higher frequencies.

In order to analyze temperature dependence of both maxima we have measured χ'' in quite low DC field of H_{DC} = 1000 Oe (Figure S17, Table S14). As is shown in the field dependence of τ (Figure S18a), in such DC field direct process is not well pronounced yet and we can consider significant contributions from Orbach and Raman processes. As can be seen on plots of thermal dependence of χ'', at low temperature (1.8 K) both maxima are observed, but they are poorly separated. With increasing temperature up to 3.6 K, maximum attributed to the faster process disappears slowly in the slope of the slower one, which clearly shifts to higher frequencies. There is the possibility that both processes of relaxation start to have the same τ or the one which disappears does not shift with temperature but just disappears in higher temperatures.

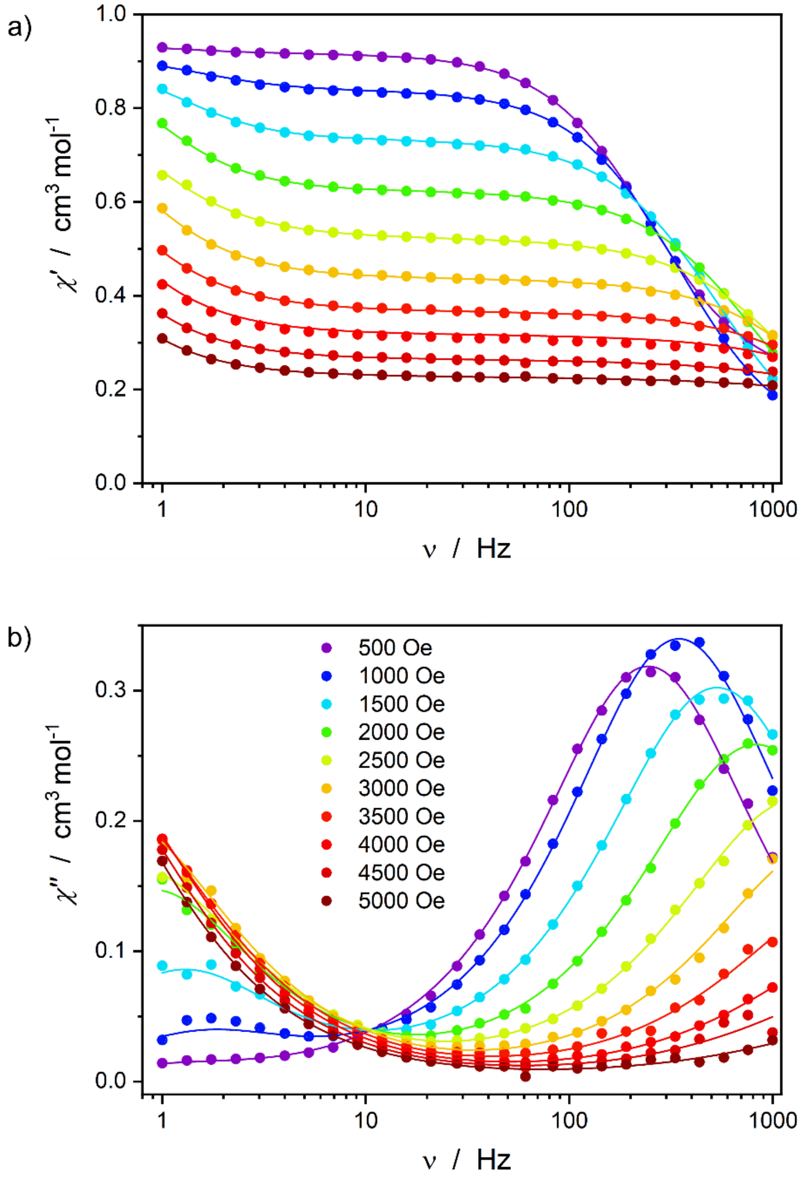

Figure S13. In-phase (χ') and out-of-phase (χ'') AC susceptibilities for **Yb** at 1.8 K measured in various fields H_{DC}. Values of α and τ parameters are presented in Table S11.

Table S11. Values of α and τ from fitting two modified Debye functions to $\tau(\nu)$ dependencies for **Yb** at 1.8 K.

***H* / Oe**	**α_1**	**τ_1 / s**
500	0.0689	$6.52(3)\cdot10^{-4}$
1000	0.0769	$4.59(4)\cdot10^{-4}$
1500	0.0942	$2.99(3)\cdot10^{-4}$
2000	0.1025	$1.91(3)\cdot10^{-4}$
2500	0.1214	$1.21(5)\cdot10^{-4}$
3000	0.1130	$8.53(78)\cdot10^{-5}$
3500	0.1438	$5.81(96)\cdot10^{-5}$

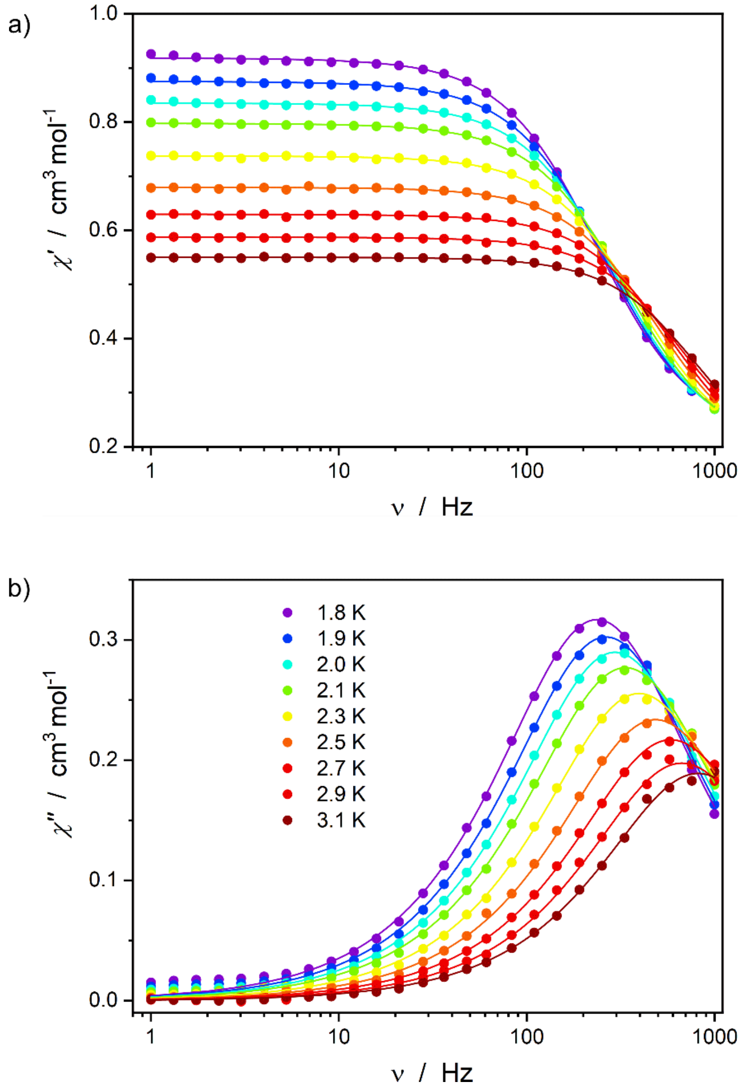

Figure S14. Temperature dependence of $\chi'(\nu)$ and $\chi''(\nu)$ for **Yb** (1-1000 Hz; H_{DC} = 500 Oe). Values of α and τ parameters are presented in Table S12.

Table S12. Values of α and τ from fitting one modified Debye function to $\tau(\nu)$ dependencies for **Yb** in H_{DC} = 500 Oe.

***T* / K**	***α***	***τ* / s**
1.8	0.0619(44)	$6.72(5)\cdot10^{-4}$
1.9	0.0582(37)	$6.03(4)\cdot10^{-4}$
2.0	0.0548(32)	$5.40(3)\cdot10^{-4}$
2.1	0.0578(30)	$4.74(3)\cdot10^{-4}$
2.3	0.0489(31)	$4.02(2)\cdot10^{-4}$
2.5	0.0477(36)	$3.29(2)\cdot10^{-4}$
2.7	0.044334)	$2.72(2)\cdot10^{-4}$
2.9	0.0359(47)	$2.38(3)\cdot10^{-4}$
3.1	0.0406(54)	$1.95(3)\cdot10^{-4}$

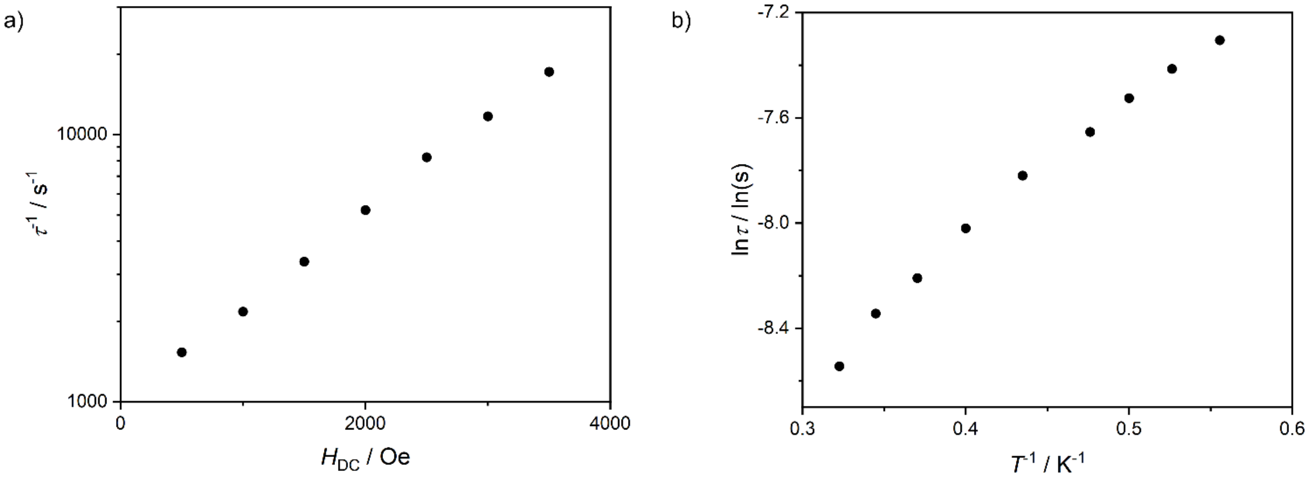

Figure S15. a) Field dependence of τ^{-1} for faster process in **Yb** at 1.8 K (500 – 3500 Oe). b) Thermal dependence of lnτ for the faster process in **Yb** under 500 Oe.

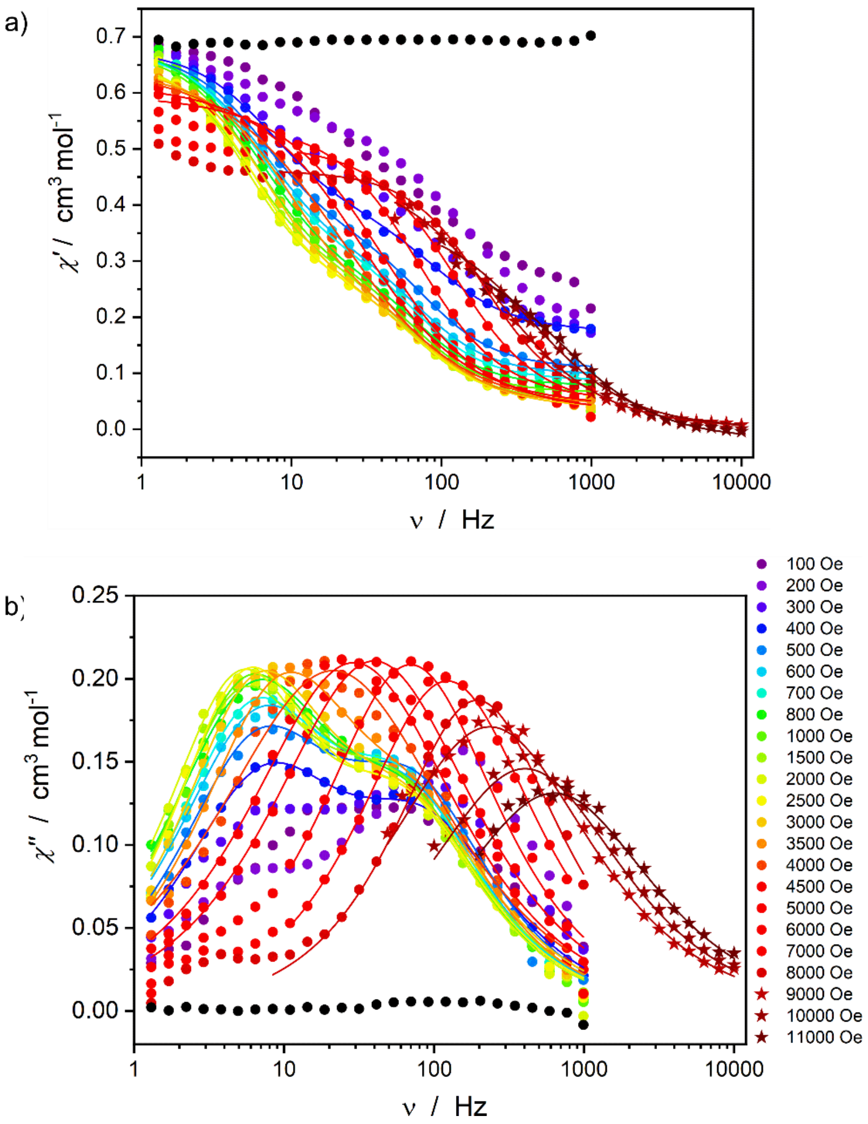

Figure S16. In-phase (χ') and out-of-phase (χ'') AC susceptibilities for **Yb2%** at 1.9 K from SQUID (circles) and PPMS (stars). Values of α and τ parameters are presented in Table S13.

Table S13. Values of α and τ from fitting two (400-3500 Oe range) or one (4000-11000 Oe range) modified Debye functions to $\tau(\nu)$ dependencies for **Yb2%** at 1.9 K.

H / Oe	**α_1**	**τ_1 / s**
400	0.0761(134)	0.0223(6)
500	0.0666(323)	0.0241(15)
600	0.0883(237)	0.0242(11)
700	0.0559(184)	0.0264(9)
800	0.1118(232)	0.0254(11)
1000	0.0494(219)	0.0283(10)
1500	0.01	0.0323(24)
2000	0.0249(270)	0.0320(12)
2500	0.0125(295)	0.0287(13)
3000	0.0398(185)	0.0244(8)
3500	0.0869(183)	0.0167(8)
	α	**τ / s**
4000	0.254(10)	0.0075(2)
4500	0.202(9)	0.0055(1)
5000	0.187(7)	0.0040(1)
6000	0.112(18)	0.0023(1)
7000	0.109(21)	$13.0(4)\cdot10^{-4}$
8000	0.0676(99)	$8.22(13)\cdot10^{-4}$
9000	0.065(15)	$5.03(13)\cdot10^{-4}$
10000	0.169(19)	$3.94(15)\cdot10^{-4}$
11000	0.171(14)	$2.52(7)\cdot10^{-4}$

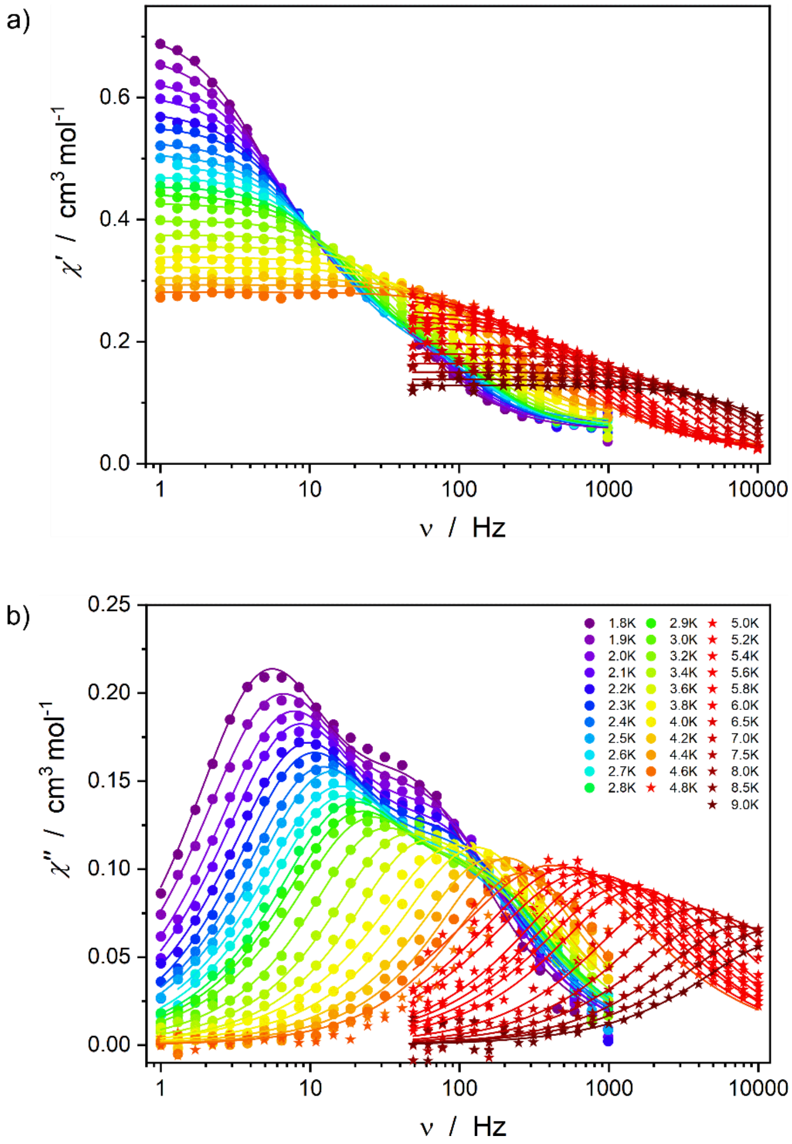

Figure S17. Temperature dependence of $\chi'(\nu)$ and $\chi''(\nu)$ for **Yb2%** (1-10000 Hz; H_{DC} = 1000 Oe). Values of α and τ parameters are presented in Table S14.

Table S14. Values of α and τ from fitting two (1.8 - 3.6 K range) or one (3.8 - 9.0 K range) modified Debye function to $\tau(\nu)$ dependencies for **Yb2%** in H_{DC} = 1000 Oe.

T / K	α_1	τ_1 / s	T / K	α	τ / s
1.8	0.051(19)	0.0328(11)	3.8	0.089(12)	$1.66(4)\cdot10^{-3}$
1.9	0.067(20)	0.0282(11)	4.0	0.065(13)	$1.23(3)\cdot10^{-3}$
2.0	0.067(15)	0.0233(7)	4.2	0.042(10)	$9.87(16)\cdot10^{-4}$
2.1	0.064(18)	0.0208(7)	4.4	0.014(17)	$7.66(21)\cdot10^{-4}$
2.2	0.062(23)	0.0186(9)	4.6	0.021(17)	$6.09(17)\cdot10^{-4}$
2.3	0.037(14)	0.0175(5)	4.8	0.204(13)	$3.85(10)\cdot10^{-4}$
2.4	0.050(11)	0.0150(4)	5.0	0.168(9)	$2.93(5)\cdot10^{-4}$
2.5	0.062(27)	0.0127(8)	5.2	0.176(12)	$2.39(5)\cdot10^{-4}$
2.6	0.060(15)	0.0116(4)	5.4	0.119(16)	$1.79(5)\cdot10^{-4}$
2.7	0.046(16)	0.0107(4)	5.6	0.128(12)	$1.48(3)\cdot10^{-4}$
2.8	0.045(16)	$9.20(38)\cdot10^{-3}$	5.8	0.129(13)	$1.23(3)\cdot10^{-4}$
2.9	0.049(17)	$8.37(39)\cdot10^{-3}$	6.0	0.109(11)	$1.00(2)\cdot10^{-4}$
3.0	0.052(31)	$7.12(67)\cdot10^{-3}$	6.5	0.090(15)	$6.27(17)\cdot10^{-5}$
3.2	0.01	$6.04(52)\cdot10^{-3}$	7.0	0.087(14)	$4.15(12)\cdot10^{-5}$
3.4	0.012(19)	$4.20(26)\cdot10^{-3}$	7.5	0.098(24)	$2.86(17)\cdot10^{-5}$
3.6	0.01	$3.07(18)\cdot10^{-3}$	8.0	0.079(33)	$2.10(19)\cdot10^{-5}$
			8.5	0.125(43)	$1.33(24)\cdot10^{-5}$
			9.0	0.109(54)	$1.11(27)\cdot10^{-5}$

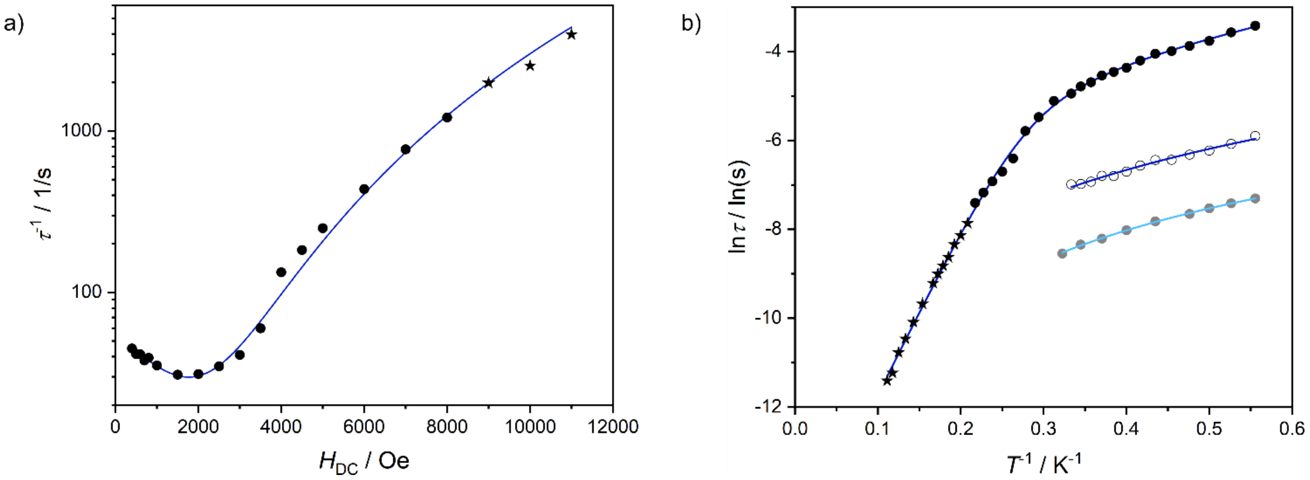

Figure S18. a) Field dependence of τ^{-1} for **Yb2%** at 1.9 K. b) Thermal dependence of τ for faster processes for **Yb** in a 500 Oe DC field (grey circles and light blue line) and for two relaxation times for **Yb2%** in a 1000 Oe DC field (one process: full circles and stars, second process: open circles; dark blue line).

Table S15. Parameters from analyses of times of slow magnetic relaxation τ for complexes from the series.

	Gd0.47%	**Er**	**Er2%**	**Yb**	**Yb2%**	
***T* /K**	1.8 K	-	1.8 K (0 - 1000 Oe) 1.9 K (1500 - 6000 Oe)	-	1.9 K	
range /Hz	1-1000	-	1 - 10000	-	1-10000	
field range /Oe	200-7000	-	0 - 6000	-	0-11000	
A_1 / s^{-1}	$8.5(3)\cdot10^{3}$	-	0 (fixed)	-	29(5)	
A_2 / Oe^{-2}	$1.13(5)\cdot10^{-5}$	-	0 (fixed)	-	$8(8)\cdot10^{-7}$	
A_3 / Oe^{-4}	$7.4(3)\cdot10^{-14}$	-	$1.76(4)\cdot10^{-11}$	-	$3.0(1)\cdot10^{-13}$	
A_4 / s^{-1}	$2.50(4)\cdot10^{2}$	-	391(9)	-	19(6)	
R^2	0.99849	-	0.99358	-	0.96909	
H_{DC} **/Oe**	3500	200	400	500	1000	
range /Hz	1-1000	1 - 1000	10 - 10000	1 - 1000	1 - 10000	
temp. range /K	1.8-4.9	1.8 – 2.9	1.9 - 5.4	1.8 – 3.1	1.8 - 9.0	1.8 - 3.6
C_1 / $s^{-1}K^{-1}$	56(1)	1002(48)	0.235 (fixed)	271(21)	0.158 (fixed)	0 (fixed)
C_2 / $s^{-1}K^{-n}$	6.2 (fixed)	51(8)	52(6)	213(6)	6.6(6)	112(8)
n	2.67(2)	3 (fixed)	2.98(12)	2.63 (fixed)	2.63(11)	2.12(8)
τ_0 / s	-	0 (fixed)	$4.4(1.5)\cdot10^{-9}$	0 (fixed)	$2.0(2)\cdot10^{-7}$	0 (fixed)
(U_{eff}/k_B) / K	-	0 (fixed)	44(2)	0 (fixed)	38(1)	0 (fixed)
R^2	0.99803	0.98654	0.99877	0.99853	0.99921	0.98598

9. EPR spectroscopy

Continuous wave and pulse EPR measurements were conducted for solid state diluted powdered samples submerged in a small amount of toluene:methanol (3:1) mixture in order to prevent sample from solvent loss. The solid state dilution was achieved similarly to that described for **Er2%** and **Yb2%**. CW X-band (9.4 GHz) spectra were acquired on a Bruker EMX spectrometer, while CW K-band (23.8 GHz) and pulse X-band (9.7 GHz) spectra were measured on Bruker Elexsys E580 spectrometers (EPSRC National UK EPR Research Facility, The University of Manchester, UK).

Microwave power, field modulation and measurement temperature in CW experiments were optimized in order to prevent sample saturation. The echo-detected field-swept EPR spectra were obtained with a Hahn echo pulse sequence ($\pi/2$-τ-π-τ-echo) under variation of the static magnetic field.

Spin-lattice relaxation times T_1 were determined with an inversion recovery sequence (π-t-$\pi/2$-τ-π-τ-echo) for variable t and $\pi/2$ chosen as either 128 ns or 16 ns, depending on the echo intensity. Field positions corresponding to the appropriate transitions were determined from the field-swept echo-detected spectra (Figures 6 and S20). The experimental data were modelled with the biexponential model:

$$I(t) = \mathrm{A}\exp(-t/T_1) + \mathrm{B}\exp(-t/T_{1.s}) + y_0 \qquad \text{(Eq. ESI1)}$$

where the longer time T_1 is assumed to be spin-lattice relaxation time and the shorter $T_{1,s}$ is spectral diffusion.[2,8–13]

Phase memory times T_m were obtained by fitting integrals of the Hahn echo decay obtained for increasing τ to the following equation:

$$I(2\tau) = \mathrm{A}\exp(-2\tau/T_m)^{\beta} + y_0 \qquad \text{(Eq. ESI2)}$$

Fit parameters of T_1 and T_m are presented in Tables S16-S20.

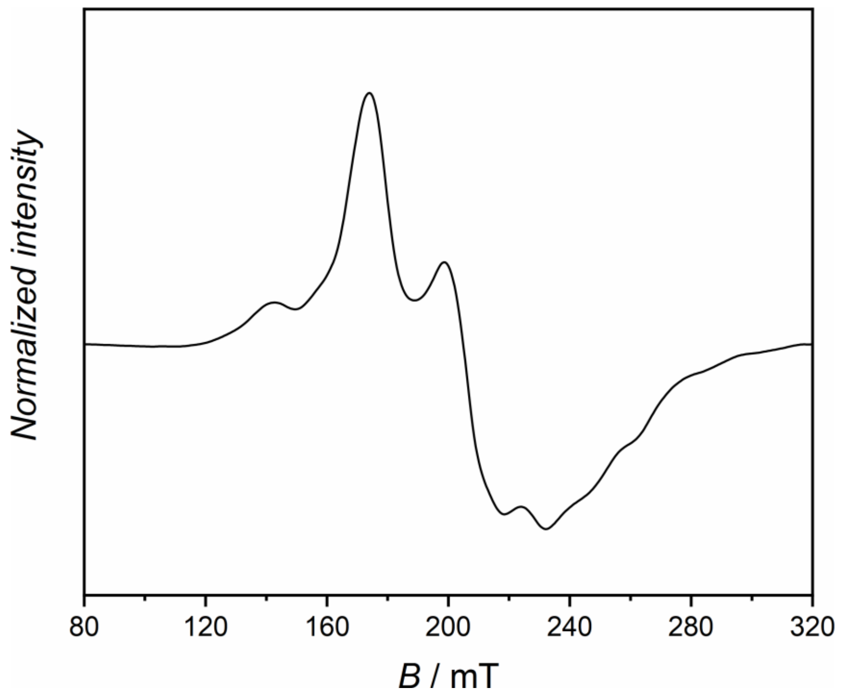

Figure S19. Continuous wave EPR spectrum of **Yb0.3%** at X-band (*T* = 8.0 K).

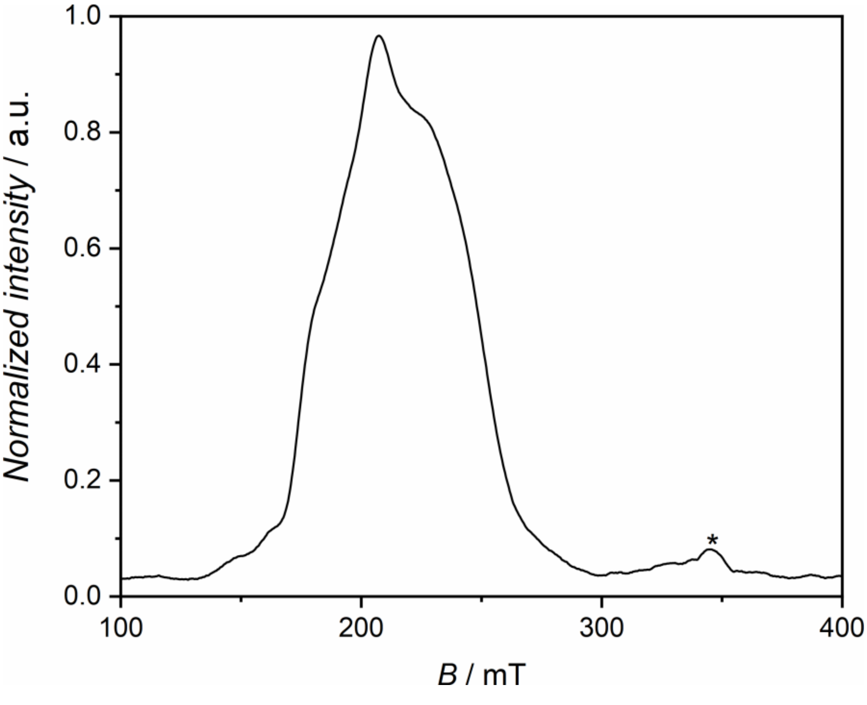

Figure S20. Field-swept echo-detected EPR spectrum of **Yb1%** at 8.0 K (π/2 pulse length of 128 ns). Asterisk denotes g = 2.0 signal of the impurity.

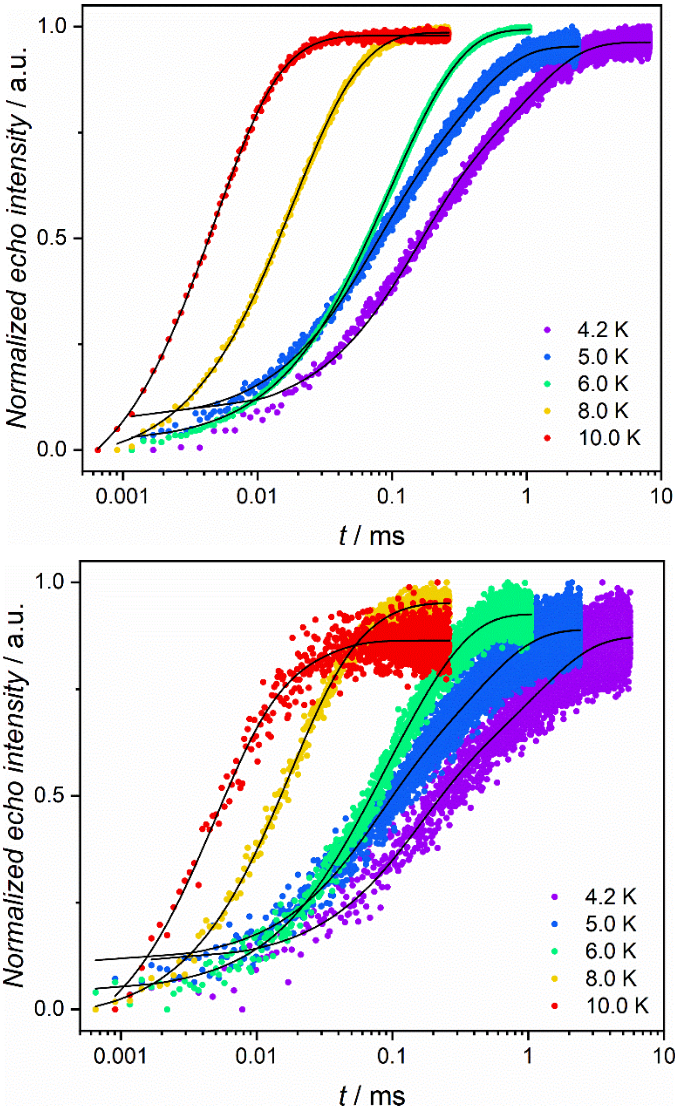

Figure S21. Normalized echo intensities as a function of time, *t*, in a standard inversion recovery sequence for **Yb1%** at temperatures for a) B = 210 mT and b) B = 176 mT ($\pi/2$ = 128 ns at 4.2 and 5.0 K, 16 ns for 6.0-10.0 K). The solid lines are best fits to the biexponential model as described in the text.

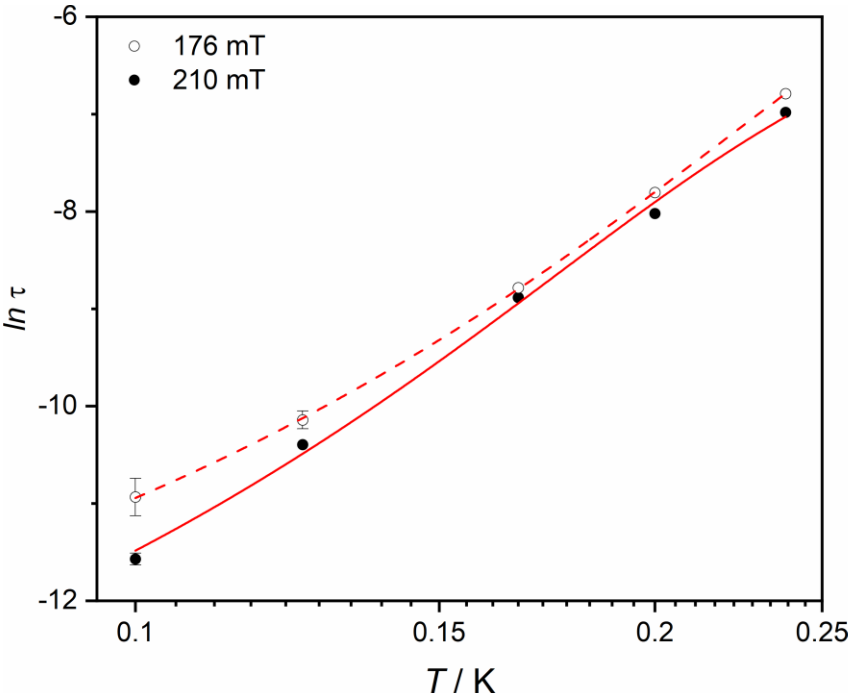

Figure S22. Temperature dependence of T_1 relaxation times for **Yb1%** at the corresponding field positions. Red lines show the best fits to the equation: $T_1^{-1} = C_2T^n + \tau_0^{-1}\exp(-U_{eff}/k_BT)$ for $n = 2.63$ obtained from AC magnetic measurements.

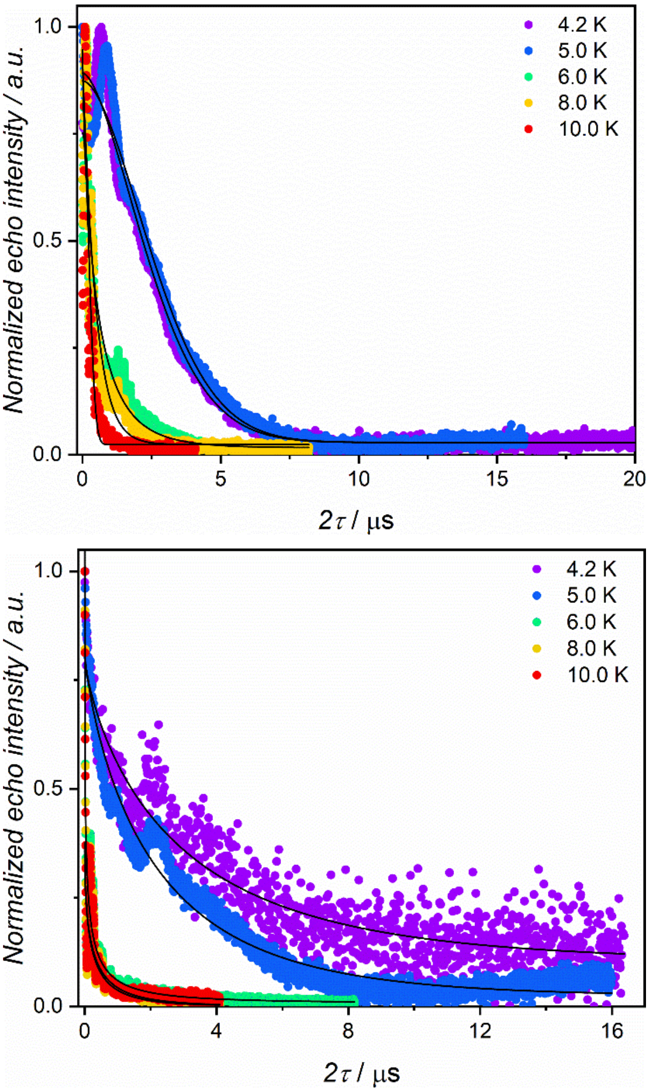

Figure S23. Normalized echo integral as a function of *2τ* for **Yb1%** at different temperatures for a) *B* = 210 mT and b) *B* = 176 mT (π/2 = 128 ns at 4.2 and 5.0 K, 16 ns for 6.0-10.0 K). The solid lines are best fits to the stretched exponential decay as described in text.

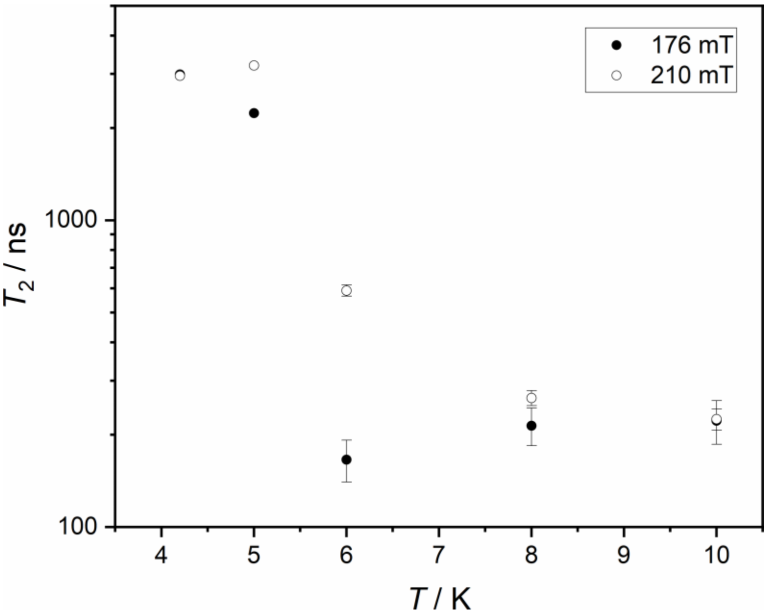

Figure S24. Thermal dependence of phase memory times T_m recorded for **Yb1%.**

Table S16. Fit parameters of T_1 to inversion recovery traces for **Yb1%** (B = 0.210 T).

	T_1 / µs	$T_{1,s}$ / µs	A	B	y_0	R^2
4.23 K	928(6)	127(2)	-0.399(3)	-0.485(3)	0.9630(2)	0.9885
5 K	328(2)	56.7(6)	-0.441(3)	-0.443(3)	0.9530(2)	0.9928
6 K	138.6(3)	43.9(4)	-0.696(3)	-0.279(3)	0.99287(7)	0.9998
8 K	30.6(7)	13.4(4)	-0.49(3)	-0.53(3)	0.9857(3)	0.9992
10 K	9.4(6)	4.1(2)	-0.32(5)	-0.79(5)	0.9787(2)	0.9965

Table S17. Fit parameters of T_1 to inversion recovery traces for **Yb1%** (B = 0.176 T).

	T_1 / µs	$T_{1,s}$ / µs	A	B	y_0	R^2
4.23 K	1126(27)	131(6)	-0.376(7)	-0.385(9)	0.873(1)	0.9031
5 K	407(6)	62(2)	-0.405(6)	-0.374(6)	0.8890(6)	0.9419
6 K	153(3)	42(3)	-0.59(2)	-0.30(2)	0.9256(7)	0.9805
8 K	39(4)	14.6(9)	-0.32(6)	-0.66(6)	0.951(1)	0.9888
10 K	18(3)	4.5(5)	-0.21(7)	-0.77(6)	0.863(1)	0.8493

Table S18. Fit parameters of T_m based on Hahn echo decay for **Yb1%** (B = 0.210 T).

	T_m / ns	β	A	y_0	R^2
4.23 K	2957(12)	1.65(2)	0.864(4)	0.0286(7)	0.9845
5 K	3196(14)	1.76(2)	0.845(4)	0.0289(9)	0.9854
6 K	590(25)	0.64(1)	0.80(2)	0	0.8849
8 K	263(15)	0.517(9)	1.12(3)	0	0.8577
10 K	225(18)	0.65(2)	0.79(4)	0	0.7555

Table S19. Fit parameters of T_m based on Hahn echo decay for **Yb1%** (B = 0.176 T).

	T_m / ns	β	A	y_0	R^2
4.23 K	2989(136)	0.77(5)	0.70(3)	0.104(9)	0.8563
5 K	2235(38)	0.79(2)	0.79(1)	0.023(2)	0.9573
6 K	166(26)	0.39(1)	0.44(4)	0	0.7429
8 K	214(30)	0.54(2)	0.36(3)	0	0.7309
10 K	222(36)	0.52(3)	0.38(3)	0	0.6964

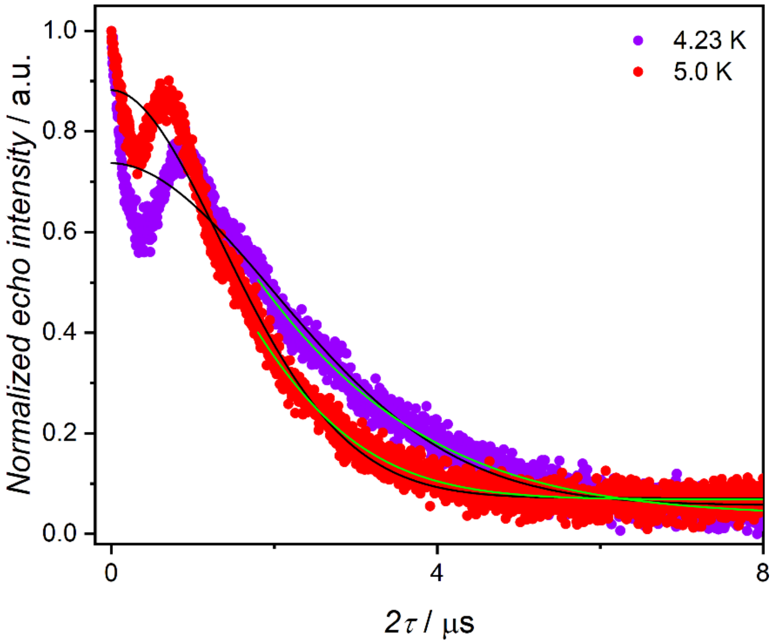

Figure S25. Normalized echo integral as a function of *2τ* for **Er0.3%** at different temperatures and *B* = 270 mT (π/2 = 128 ns). The solid lines are best fits to the stretched exponential decay as described in text - black lines show fits to the full measurement range, while green lines depict fits to 1.8-8.0 μs range (part, where electron spin echo envelope modulation is negligible).

Table S20. Fit parameters of T_m based on Hahn echo decay for **Er0.3%** (*B* = 0.27 T).

	T_m / ns	β	A	y_0	R^2
4.23 K	2964(16)	1.89(3)	0.680(4)	0.057(2)	0.9714
5 K	2022(7)	1.88(2)	0.811(3)	0.0713(7)	0.9839
4.23 K (1.8-8.0 μs range)	2501(89)	1.29(6)	0.90(5)	0.037(2)	0.9767
5 K (1.8-8.0 μs range)	1985(98)	1.60(9)	0.78(6)	0.0685(5)	0.9205

10. Ab initio calculations

Single point CASSCF/RASSI/SINGLE_ANISO calculations were carried out in OpenMolcas software (ver. 19.11).[14–16] Low temperature scXRD structural models of the $[Ln^{III}(phendo)_4]^{3+}$ complexes were used for calculations. State average CASSCF(11,7) calculations for **Er** included 35 quartet and 112 dublet spin states while CASSCF(13,7) for **Yb** used 7 dublet spin states. All calculated roots were used for spin orbit coupling in RASSI program. The models did not include structurally disordered NO_3^- anions, however, in order to simulate their effect on **Er**, two F^- anions were placed 5 Å above and below the metal atom along the C_4 symmetry axis instead of NO_3^- (**ER_F$_2$**). Scalar-relativistic Douglas-Kroll-Hess (DKH) Hamiltonian[17,18] was used with a relativistic ANO-RCC basis sets available in OpenMolcas (Tables S21, S22).[19,20] While computing two electron integrals, Cholesky decomposition with a 1.0×10^{-8} threshold was used to save disk space. The wavefunctions used in the calculations were initially optimized with minimal ANO-RCC basis set. These optimized wavefunctions were expanded with EXPBAS (Molcas module) to larger bases and used as a starting point. The results of the calculations are collected in Tables S23 and S24 for **Er** and Table S25 and S26 for **Yb**. States composition of the ground state $^4I_{15/2}$ and $^2F_{7/2}$ multiplets of **Er** and **Yb** are presented in Tables S24 and S26, respectively.

The calculations qualitatively agree with the EPR experiments. They support strong axiality of the **Er** complex caused by the propeller-like phendo ligands coordination scaffold. However, they also show that the state geometry of these complexes is not ideal for high-performance SIM as evidenced by the constitution of the ground Kramers dublet with predominant $|\pm 13/2>$ m_J character. Moreover, calculations suggests that by increasing the basis set size the results only further diverge from the experimental values (ie. $g_z = 13.64$ $g_{x,y} = 1.08$ in basis **B** and $g_z = 13.68$ $g_{x,y} = 1.04$ in basis **C** vs experimental $g_z = 11.54$ and $g_{x,y} = 2.63$), suggesting that the molecular model selected for calculations does not encapsulate the key features of the real system. The observed inconsistencies could be explained by the impact of NO_3^- anions surrounding the $[Er(phendo)_4]^{3+}$ complex. These anions were not included in early calculations (**B** and **C**) due to their severe structural disorder causing calculations instability. Preliminary geometry optimizations of models containing those anions suggested that to obtain proper geometry of the system, more extensive fragments of a crystallographic unit cell would have to be used. Therefore, due to the lack of molecular models including reliable NO_3^- positions, we have carried out additional simplified calculation **ER_F$_2$** to show that inclusion of anions in the model is indeed necessary and leads to improved results. Thus, the molecular fragment $[Er(phendo)_4]^{3+}$ complex was modified by adding two F^- anions at the C_4 rotation axis above and below the Er^{III} center with the Er-F distance of 5 Å. The distance of 5 Å was selected arbitrarily to be within the range of the most probable position of NO_3^- anions. The calculations for **ER_F$_2$** model were carried with the basis set analogous to **B** and shows a small change in the nature of the ground state. Nonetheless, this change is in line with our reasoning, because the *g* tensor of this state ended up with larger transverse and smaller axial components. Moreover, the strongly axial first excited state was destabilized. Due to a very small tunneling gap evidenced by a tiny g_x and g_y components, the first excited state (consisting mainly of $|\pm 15/2>$ m_J), would not explain the experimental U_{eff} of the magnetic relaxation and thus, upon computational model improvement, it is expected to change positions with states possessing much larger transverse *g* components responsible for the fast tunneling of the magnetization. The calculated main anisotropy axes align well with the C_4 axis of the complex. Obtained computational data supports the prolate nature of the ground state electron density in **Er**.

In case of **Yb** complex, the calculations showed small dependence on the basis set used, observed most easily in the energy gaps between the ground and the first excited states, which differ by 2 cm^{-1} between basis set **B** and **C** calculations. In both cases the first excited state is very low lying and characterized by $g_z = 4.6$ and $g_{x,y} = 2.6$, thus containing significant transverse *g* components similar to the experimentally determined *g* values. It is expected that inclusion of the axially placed anions NO_3^- and the dynamic electron correlation would cause the strongly axial anisotropic ground state to switch places with the first excited state. To summarize, the poor agreement of the **Yb** calculations with the experiment may be ascribed to the lack of NO_3^- anions in the molecular model selceted for calculations.

Table S21. Basis sets used in CASSCF calculation for **Er**.

ANO-RCC-…	**A**	**B**	**C**	MODEL **ER_F$_2$**
Er	6s5p3d1f MB	7s6p4d2f1g VDZP	8s7p5d3f2g1h VTZP	7s6p4d2f1g VDZP
O*	2s1p MB	3s2p1d VDZP	4s3p2d1f VTZP	3s2p1d VDZP
N	2s1p MB	3s2p VDZ	3s2p1d VDZP	3s2p VDZ
C	2s1p MB	3s2p VDZ	3s2p1d VDZP	3s2p VDZ
H	1s MB	2s VDZ	2s1p VDZP	2s VDZ
F**	2s1p MB	-	-	2s1p MB

*atoms directly bonded with Er

**F$^-$ was used in some calculations to simulate influence of structurally disordered NO_3^- anions on the crystal field of the complex.

Table S22. Basis sets used in CASSCF calculation for **Yb**.

ANO-RCC-....	**A**	**B**	**C**
YB	6s5p3d1f MB	7s6p4d2f1g VDZP	8s7p5d3f2g1h VTZP
O*	2s1p MB	3s2p VDZ	3s2p1d VDZP
N	2s1p MB	3s2p VDZ	3s2p1d VDZP
C	2s1p MB	3s2p VDZ	3s2p1d VDZP
H	1s MB	2s VDZ	2s1p VDZP

*atoms directly bonded with Yb

Table S23. Ab initio calculated energy spectrum and g tensors for **Er**.

KD	g tensor	Basis B		Basis C		Model Er_F_2	
		g	E /cm^{-1}	g	E /cm^{-1}	g	E /cm^{-1}
1	$g_{x,y}^*$	1.08	0.00	1.04	0.00	1.30	0.00
	g_z	13.64		13.68		13.42	
2	$g_{x,y}$	0.015	34.39	0.016	34.12	0.035	48.55
	g_z	16.79		16.83		16.58	
3	$g_{x,y}$	0.66	89.19	0.61	90.55	0.86	78.48
	g_z	8.54		8.47		8.17	
4	$g_{x,y}$	8.45	138.8	8.54	136.9	8.55	119.6
	g_z	2.40		2.30		2.26	
5	$g_{x,y}$	6.07	291.0	5.93	292.2	5.88	277.2
	g_z	5.31		5.52		5.68	
6	$g_{x,y}$	0.48	305.5	0.38	309.9	0.39	293.0
	g_z	9.47		9.56		9.60	
7	$g_{x,y}$	6.49	335.7	6.35	336.8	6.31	319.7
	g_z	5.01		5.11		5.23	
8	$g_{x,y}$	0.70	346.0	0.71	350.1	0.67	334.4
	g_z	9.42		9.38		9.63	

Table S24. State composition for each Kramer Doublet (KD) of the ground $^4I_{15/2}$ **Er** multiplet.

<table>
<tr><th rowspan="2">KD</th><th colspan="6">|m_j> Composition in %</th></tr>
<tr><th colspan="2">Basis B</th><th colspan="2">Model Er_F_2</th><th colspan="2">Basis C</th></tr>
<tr><td>1</td><td>|-13/2> 49.8
|-11/2> 0.1
|-5/2> 11.1
|-3/2> 0.2
|+3/2> 0.3
|+5/2> 7.0
|+11/2> 0.1
|+13/2> 31.3</td><td>|-13/2> 31.3
|-11/2> 0.1
|-5/2> 7.0
|-3/2> 0.3
|+3/2> 0.2
|+5/2> 11.1
|+11/2> 0.1
|+13/2> 49.8</td><td>|-13/2> 24.9
|-11/2> 0.2
|-5/2> 6.2
|-3/2> 0.5
|+3/2> 0.2
|+5/2> 13.6
|+11/2> 0.1
|+13/2> 54.3</td><td>|-13/2> 54.3
|-11/2> 0.1
|-5/2> 13.6
|-3/2> 0.2
|+3/2> 0.5
|+5/2> 6.2
|+11/2> 0.2
|+13/2> 24.9</td><td>|-13/2> 30.5
|-11/2> 0.1
|-5/2> 6.7
|-3/2> 0.3
|+3/2> 0.2
|+5/2> 11.1
|+11/2> 0.1
|+13/2> 51.0</td><td>|-13/2> 51.0
|-11/2> 0.1
|-5/2> 11.1
|-3/2> 0.2
|+3/2> 0.3
|+5/2> 6.7
|+11/2> 0.1
|+13/2> 30.5</td></tr>
<tr><td>2</td><td>|-15/2> 88.3
|-7/2> 11.7</td><td>|+7/2> 11.7
|+15/2> 88.3</td><td>|-15/2> 1.2
|-7/2> 0.2
|-1/2> 0.1
|+7/2> 13.7
|+15/2> 84.9</td><td>|-15/2> 84.9
|-7/2> 13.7
|+1/2> 0.1
|+7/2> 0.2
|+15/2> 1.2</td><td>|-15/2> 81.8
|-7/2> 10.4
|+7/2> 0.9
|+15/2> 6.9</td><td>|-15/2> 6.9
|-7/2> 0.9
|+7/2> 10.4
|+15/2> 81.8</td></tr>
<tr><td>3</td><td>|-13/2> 1.0
|-11/2> 0.9
|-5/2> 0.1
|-3/2> 0.7
|+3/2> 44.1
|+11/2> 53.1</td><td>|-11/2> 53.1
|-3/2> 44.1
|+3/2> 0.7
|+5/2> 0.1
|+11/2> 0.9
|+13/2> 1.0</td><td>|-11/2> 50.6
|-3/2> 47.8
|+3/2> 0.1
|+11/2> 0.1
|+13/2> 1.4</td><td>|-13/2> 1.4
|-11/2> 0.1
|-3/2> 0.1
|+3/2> 47.8
|+11/2> 50.6</td><td>|-13/2> 0.5
|-11/2> 23.8
|-3/2> 20.5
|+3/2> 25.3
|+11/2> 29.3
|+13/2> 0.4</td><td>|-13/2> 0.4
|-11/2> 29.3
|-3/2> 25.3
|+3/2> 20.5
|+11/2> 23.8
|+13/2> 0.5</td></tr>
<tr><td>4</td><td>|-1/2> 0.3
|+1/2> 87.0
|+9/2> 12.6</td><td>|-9/2> 12.6
|-1/2> 87.0
|+1/2> 0.3</td><td>|-15/2> 0.1
|-9/2> 3.0
|-1/2> 23.9
|+1/2> 64.8
|+9/2> 8.2</td><td>|-9/2> 8.2
|-1/2> 64.8
|+1/2> 23.9
|+9/2> 3.0
|+15/2> 0.1</td><td>|-9/2> 11.6
|-1/2> 88.2
|+1/2> 0.1</td><td>|-1/2> 0.1
|+1/2> 88.2
|+9/2> 11.6</td></tr>
<tr><td>5</td><td>|-13/2> 0.5
|-11/2> 34.7
|-5/2> 1.8
|-3/2> 36.6
|+3/2> 5.5
|+5/2> 12.1
|+11/2> 5.2
|+13/2> 3.5</td><td>|-13/2> 3.5
|-11/2> 5.2
|-5/2> 12.1
|-3/2> 5.5
|+3/2> 36.6
|+5/2> 1.8
|+11/2> 34.7
|+13/2> 0.5</td><td>|-13/2> 1.0
|-11/2> 32.5
|-5/2> 3.1
|-3/2> 30.2
|+3/2> 9.8
|+5/2> 9.7
|+11/2> 10.6
|+13/2> 3.1</td><td>|-13/2> 3.1
|-11/2> 10.6
|-5/2> 9.7
|-3/2> 9.8
|+3/2> 30.2
|+5/2> 3.1
|+11/2> 32.5
|+13/2> 1.0</td><td>|-13/2> 3.2
|-11/2> 6.3
|-5/2> 11.2
|-3/2> 6.5
|+3/2> 35.5
|+5/2> 2.0
|+11/2> 34.7
|+13/2> 0.6</td><td>|-13/2> 0.6
|-11/2> 34.7
|-5/2> 2.0
|-3/2> 35.5
|+3/2> 6.5
|+5/2> 11.2
|+11/2> 6.3
|+13/2> 3.2</td></tr>
<tr><td>6</td><td>|-9/2> 1.0
|-7/2> 0.3
|-1/2> 0.1
|+1/2> 12.3
|+9/2> 86.2</td><td>|-9/2> 86.2
|-1/2> 12.3
|+1/2> 0.1
|+7/2> 0.3
|+9/2> 1.0</td><td>|-9/2> 80.6
|-1/2> 10.1
|+1/2> 1.0
|+7/2> 0.2
|+9/2> 8.0</td><td>|-9/2> 8.0
|-7/2> 0.2
|-1/2> 1.0
|+1/2> 10.1
|+9/2> 80.6</td><td>|-9/2> 88.1
|-1/2> 11.5
|+7/2> 0.3
|+9/2> 0.1</td><td>|-9/2> 0.1
|-7/2> 0.3
|+1/2> 11.5
|+9/2> 88.1</td></tr>
<tr><td>7</td><td>|-13/2> 0.5
|-11/2> 5.6
|-5/2> 2.5
|-3/2> 12.0
|+3/2> 0.4
|+5/2> 65.5
|+11/2> 0.2
|+13/2> 13.3</td><td>|-13/2> 13.3
|-11/2> 0.2
|-5/2> 65.5
|-3/2> 0.4
|+3/2> 12.0
|+5/2> 2.5
|+11/2> 5.6
|+13/2> 0.5</td><td>|-13/2> 15.3
|-5/2> 67.3
|+3/2> 11.3
|+5/2> 0.1
|+11/2> 6.0</td><td>|-11/2> 6.0
|-5/2> 0.1
|-3/2> 11.3
|+5/2> 67.3
|+13/2> 15.3</td><td>|-13/2> 0.1
|-11/2> 5.6
|-5/2> 0.6
|-3/2> 11.6
|+3/2> 0.1
|+5/2> 68.3
|+13/2> 13.6</td><td>|-13/2> 13.6
|-5/2> 68.3
|-3/2> 0.1
|+3/2> 11.6
|+5/2> 0.6
|+11/2> 5.6
|+13/2> 0.1</td></tr>
<tr><td>8</td><td>|-9/2> 0.2
|-7/2> 0.1
|-1/2> 0.2
|+7/2> 87.9
|+15/2> 11.6</td><td>|-15/2> 11.6
|-7/2> 87.9
|+1/2> 0.2
|+7/2> 0.1
|+9/2> 0.2</td><td>|-15/2> 13.2
|-7/2> 82.0
|+1/2> 0.1
|+7/2> 3.9
|+9/2> 0.2
|+15/2> 0.6</td><td>|-15/2> 0.6
|-9/2> 0.2
|-7/2> 3.9
|-1/2> 0.1
|+7/2> 82.0
|+15/2> 13.2</td><td>|-9/2> 0.2
|-1/2> 0.2
|+7/2> 88.4
|+15/2> 11.2</td><td>|-15/2> 11.2
|-7/2> 88.4
|+1/2> 0.2
|+9/2> 0.2</td></tr>
</table>

*only components with non-zero contribution are shown

Table S25. Ab initio calculated energy spectrum and g tensors for **Yb**.

KD	g tensor	**Basis B**		**Basis C**	
		g	E /cm^{-1}	g	E /cm^{-1}
1	$g_{x,y}$	0.0003, 0.0004	0.00	0.001, 0.002	0.00
	g_z	7.984		7.982	
2	$g_{x,y}$	2.61	6.25	2.62	2.85
	g_z	4.59		4.58	
3	$g_{x,y}$	2.60	349.9	2.60	375.0
	g_z	2.29		2.28	
4	$g_{x,y}$	4.56	400.12	4.56	421.7
	g_z	1.14		1.14	

Table S26. State composition for each Kramer Doublet (KD) of the ground $^2F_{7/2}$ **Yb** multiplet.

KD	**|m$_j$> Composition in %**			
	Basis **B**		Basis **C**	
1	|+7/2> 99.9	|-7/2> 99.9 |-5/2> 27.9 |-3/2> 9.7 |+3/2> 4.7 |+5/2> 57.8	|-7/2> 66 |+7/2> 34	|-7/2> 34 |+7/2> 66
2	|-5/2> 86.3 |-3/2> 0.2 |+3/2> 11.9 |+5/2> 1.6	|-5/2> 1.6 |-3/2> 11.9 |+3/2> 0.2 |+5/2> 86.3	|-5/2> 87.2 |-3/2> 0.1 |+3/2> 12.1 |+5/2> 0.6	|-5/2> 0.6 |-3/2> 12.1 |+3/2> 0.1 |+5/2> 87.2
3	|-5/2> 1.6 |-3/2> 76.5 |+3/2> 11.4 |+5/2> 10.5	|-5/2> 10.5 |-3/2> 11.4 |+3/2> 76.5 |+5/2> 1.6	|-5/2> 1.9 |-3/2> 73.8 |+3/2> 14.0 |+5/2> 10.3	|-5/2> 10.3 |-3/2> 14.0 |+3/2> 73.8 |+5/2> 1.9
4	|-1/2> 99.9 |+1/2> 0.3	|-1/2> 0.3 |+1/2> 99.7	|-1/2> 100	|+1/2> 100

*only components with non-zero contribution are shown

References

1 S. Rozen and S. Dayan, *Angew. Chem. Int. Ed.*, 1999, **38**, 3471–3473.

2 G. Handzlik, M. Magott, M. Arczyński, A. M. Sheveleva, F. Tuna, M. Sarewicz, A. Osyczka, M. Rams, V. Vieru, L. F. Chibotaru and D. Pinkowicz, *J. Phys. Chem. Lett.*, 2020, 1508–1515.

3 G. M. Sheldrick, *Acta Crystallogr. Sect. A*, 2008, **64**, 112–122.

4 O. V Dolomanov, L. J. Bourhis, R. J. Gildea, J. A. K. Howard and H. Puschmann, *J. Appl. Crystallogr.*, 2009, **42**, 339–341.

5 M. Llunell, D. Casanova, J. Cirera, P. Alemany and S. Alvarez, *Univ. Barcelona, Barcelona, Spain*.

6 G. A. Bain and J. F. Berry, *J. Chem. Educ.*, 2008, **85**, 532.

7 Y.-N. Guo, G.-F. Xu, Y. Guo and J. Tang, *Dalton Trans.*, 2011, **40**, 9953.

8 K. Bader, M. Winkler and J. van Slageren, *Chem. Commun.*, 2016, **52**, 3623–3626.

9 S. Takahashi, J. van Tol, C. C. Beedle, D. N. Hendrickson, L.-C. Brunel and M. S. Sherwin, *Phys. Rev. Lett.*, 2009, **102**, 87603.

10 K. S. Pedersen, A.-M. Ariciu, S. McAdams, H. Weihe, J. Bendix, F. Tuna and S. Piligkos, *J. Am. Chem. Soc.*, 2016, **138**, 5801–5804.

11 T. Yamabayashi, M. Atzori, L. Tesi, G. Cosquer, F. Santanni, M.-E. Boulon, E. Morra, S. Benci, R. Torre, M. Chiesa, L. Sorace, R. Sessoli and M. Yamashita, *J. Am. Chem. Soc.*, 2018, **140**, 12090–12101.

12 J. M. Zadrozny, J. Niklas, O. G. Poluektov and D. E. Freedman, *ACS Cent. Sci.*, 2015, **1**, 488–492.

13 M. Atzori, A. Chiesa, E. Morra, M. Chiesa, L. Sorace, S. Carretta and R. Sessoli, *Chem. Sci.*, 2018, **9**, 6183–6192.

14 F. Aquilante, J. Autschbach, R. K. Carlson, L. F. Chibotaru, M. G. Delcey, L. De Vico, I. Fdez. Galván, N. Ferré, L. M. Frutos, L. Gagliardi, M. Garavelli, A. Giussani, C. E. Hoyer, G. Li Manni, H. Lischka, D. Ma, P. Å. Malmqvist, T. Müller, A. Nenov, M. Olivucci, T. B. Pedersen, D. Peng, F. Plasser, B. Pritchard, M. Reiher, I. Rivalta, I. Schapiro, J. Segarra-Martí, M. Stenrup, D. G. Truhlar, L. Ungur, A. Valentini, S. Vancoillie, V. Veryazov, V. P. Vysotskiy, O. Weingart, F. Zapata and R. Lindh, *J. Comput. Chem.*, 2016, **37**, 506–541.

15 B. O. Roos, P. R. Taylor and P. E. M. Sigbahn, *Chem. Phys.*, 1980, **48**, 157–173.

16 P. Å. Malmqvist, B. O. Roos and B. Schimmelpfennig, *Chem. Phys. Lett.*, 2002, **357**, 230–240.

17 M. Douglas and N. M. Kroll, *Ann. Phys. (N. Y).*, 1974, **82**, 89–155.

18 B. A. Hess, *Phys. Rev. A*, 1986, **33**, 3742–3748.

19 B. O. Roos, R. Lindh, P.-Å. Malmqvist, V. Veryazov and P.-O. Widmark, *J. Phys. Chem. A*, 2005, **109**, 6575–6579.

20 B. O. Roos, R. Lindh, P.-Å. Malmqvist, V. Veryazov and P.-O. Widmark, *J. Phys. Chem. A*, 2004, **108**, 2851–2858.